

**CHAPTER 5**  
**CHARACTERIZATION OF GEOLOGICAL MATERIALS**  
**USING ION AND PHOTON BEAMS**

Sz. B. Török  
Atomic Energy Research Institute, Budapest, H-1525 Hungary

K. W. Jones  
Brookhaven National Laboratory, Upton, New York 11973-5000 USA

C. Tuniz  
Australian Nuclear Science & Technology Organization, Lucas Heights, NSW 2234, Menai, Australia

Published in

Nuclear Materials in Mineralogy and Geology: Techniques and Applications

Edited by

A. Vértes, S. Nagy, and K. Süvegh

Plenum Press, New York

1998



## 5

### CHARACTERIZATION OF GEOLOGICAL MATERIALS USING ION AND PHOTON BEAMS

SZ. B. TÖRÖK, K. W. JONES, and C. TUNIZ

#### INTRODUCTION

Geological specimens are often complex materials that require different analytical methods for their characterization. The parameters of interest may include the chemical composition of major, minor and trace elements. The chemical compounds incorporated in the minerals, the crystal structure and isotopic composition need to be considered. Specimens may be highly heterogeneous thus necessitating analytical methods capable of measurements on small sample volumes with high spatial resolution and sensitivity. Much essential information on geological materials can be obtained by using ion or photon beams. In this chapter we describe the principal analytical techniques based on particle accelerators, showing some applications that are hardly possible with conventional methods.

In particular, the following techniques will be discussed:

1. Synchrotron radiation (SR) induced X-ray emission (SRIXE) and particle-induced X-ray emission (PIXE) and other ion beam techniques for trace element analysis.
2. Accelerator mass spectrometry (AMS) for ultra sensitive analysis of stable nuclides and long-lived radionuclides.

In most of the cases also the possibilities of elemental and isotopic analysis with high resolution will be discussed.

#### 5.1. SYNCHROTRON RADIATION ANALYSIS

##### 5.1.1. Synchrotron radiation facilities

The extreme brightness of SR sources makes them particularly relevant to the investigation of minerals and other geological materials. While the first X-ray beams were generated almost 100 years ago from the cathode of an X-ray tube, over the following 60 years there was little development in the performance of X-ray sources. The rotating anode gave a noticeable enhancement of source brilliance but the most significant step towards high brilliance sources was the use of storage rings for synchrotron radiation research. During the 1980's insertion devices consisting of alternating magnetic fields along the straight sections of the orbit (causing the

---

SZ. B. TÖRÖK • Atomic Energy Research Institute, Budapest, P.O.B. 49, H-1525, Hungary

K. W. JONES • Brookhaven National Laboratory, DAS Upton, NY 11973, USA

C. TUNIZ • Australian Nuclear Science & Technology Organization, Lucas Heights, NSW 2234, PMB 1, Menai, Australia

charged particle to execute small deviations in the trajectory) came into use. The third generation SR facilities are mainly based on insertion devices that offer the possibility of extremely high brilliance sources with unique characteristics; wavelength tunability from the infrared to hard X-rays, high degree of polarization and selectivity as well as source coherence. These X-ray sources allow the development of experimental facilities with ultra-high sensitivity for chemical analysis.

Since the first experiments carried out at SPEAR (Stanford) to characterize geological samples, many experimental stations were developed at SR facilities for this kind of research and geologists joined the wide community of SR users. Table 5.1.1 presents the SR sources where mineral analysis was reported.

Table 5.1.1  
SR photon sources where mineral analysis was reported

Location	Ring (Inst.)	Electron Energy (GeV)	Notes
Stanford (CA, USA)	SPEAR	3-3.5	first generation
Ithaca (NY, USA)	CHASS	5.5	first generation
Hamburg (Germany)	HASYLAB	3.5	first generation
Orsay (France)	DCI	1.8	first generation
Novosibirsk (FSU)	VEPP-3	2.2	first generation
Daresby (UK)	SRS	2	second generation
Tsukuba (Japan)	KEK	2.5	second generation
Upton, NY	NSLS	2.5	second generation
Berkeley, CA	ALS (LBL)	1.5	third generation
Grenoble (France)	ESRF	6	third generation
Trieste (Italy)	ELETTRA	2.0	third generation
Hsinchu (Taiwan)	SRRC	1.3	third generation
Argonne (IL, USA)	APS	7	third generation

Here we briefly report on the world-wide commissioning of new SR facilities. In the following sections we'll discuss the properties of SR and some X-ray fluorescence (XRF) experiments with SR microbeams.

A hard X-ray source, the European Synchrotron Radiation Facility (ESRF), was successfully commissioned in December 1992 at 100 mA current in multi-bunch mode with 12 hours lifetime. Third generation hard X-ray sources are being constructed at the Argonne National Laboratory (APS) and in Japan (Spring-8) [1].

The Advanced Light Source at the Lawrence Berkeley Laboratory has been commissioned in 1993 [2]. Since that time a 400 mA current was reached for multi-bunch mode. Undulator fluorescence beam lines (2 to 10 keV) and bending magnet beam lines became available in 1994.

A high brightness VUV/soft X-ray synchrotron radiation facility, ELETTRA, has been commissioned recently in Trieste. The instrumental and design parameters of the 2 GeV source were reviewed by Walker [3].

A source with similar energy range is under construction in Moscow designed by the Siberian group. Commissioning of the machine was scheduled for 1994 [4]. A few other sources planned for basic and applied science are under construction or in the design stage [5, 6]. It is worth mentioning that Helios, the compact source of Oxford Instruments is already installed at IBM's Advanced Lithography Facility and is running routinely since January 1992 [7, 8].

In 1992 the Photon Factory celebrated the 10<sup>th</sup> anniversary of the 2.5 GeV storage rings where on the 3 T superconducting wiggler line the critical photon energy is 20 keV [9].

### 5.1.2. Properties of synchrotron radiation

It has been known since Röntgen's discovery that the acceleration of charged particles results in the emission of electromagnetic radiation. Almost fifty years later Elder [10] and coworkers discovered that relativistic electrons orbiting in circular path emit very intense electromagnetic radiation in the UV or X-ray energy range (synchrotron radiation).

Synchrotron produced X-ray beams have unique properties that make them desirable for use in high-sensitivity analysis of geological materials:

1. The broad spectral range with continuous energy distribution produced by a SR bending magnet is suitable to produce monoenergetic beams over a wide range of energies.
2. The high degree of polarization in the plane of the electron orbit is extremely important for background reduction in SRIXE experiments
3. The high-intensity X-ray flux emitted by the bending magnet is characterised by a natural collimation in the vertical direction and intense beams with little angular divergence can be produced. In addition, the high brilliance of the source allows the focusing of very intense beams over a small area.

In order to understand the reason of high brilliance of synchrotron radiation we should consider the radiation emitted by accelerated electrons. At non relativistic energies, electrons in circular motion radiate a torus-shaped dipole pattern as shown in Figure 5.1.1a. At relativistic energies this pattern becomes sharply peaked in the direction of motion as presented in Figure 5.1.1b. Any photon used in an experiment in the reference frame of the laboratory undergoes a transformation governed by special relativity. The high-speed electron in a synchrotron emits a very narrow jet which becomes even more brilliant with increasing energy. Light emitted at an angle  $\theta$  relative to the electron direction of motion in the rest frame is viewed at an angle  $\theta'$  in the laboratory frame. The transformation valid near the critical energy is given by

$$\tan\theta' = \frac{\sin\theta}{\gamma(\beta + \cos\theta)}, \quad \text{where } \gamma = \frac{E}{mc^2}, \beta = v/c. \quad (5.1.1)$$

At  $\theta=90^\circ$   $\tan\theta' \approx \theta' \approx \gamma^{-1}$  is the emission half angle in the laboratory system. This opening angle is 500  $\mu\text{rad}$  for 1 GeV electron energy and 73  $\mu\text{rad}$  at 7 GeV.

Basically there are three figures of merit that are necessary in the design of an experiment at a SR beam line. The **flux** is the number of photons/s/horizontal angle. This value is relevant for a large sample intercepting the entire beam in the horizontal angle. The **brightness** is the number of photons/vertical angle. This value is relevant for pinhole experiments. The **brilliance** is the brightness/source area that has to be considered in the designs using optical imaging.

First-generation hard X-ray sources were "parasitic" on accelerators used for high energy physics. The bending magnets for X-ray production were fitted into parts of existing rings. When an electron bunch passes through a bending magnet the horizontal divergence is increased by the arc subtended by the magnet at the center of the curvature. Assuming that the size and angular divergence of the electron beam are not important the source brightness (in units of photons/s/mrad<sup>2</sup>/0.1%BW) is given according to [11]:

$$B_{BM} = 1.33 \times 10^{13} E^2 I H_2(\epsilon/\epsilon_c) \quad (5.1.2)$$

where  $E$  is the electron energy in gigaelectronvolts,  $I$  is the electron current in amperes,  $\epsilon$  is the X-ray energy,  $\epsilon_c$  is the critical energy of the storage ring and  $H_2(\epsilon/\epsilon_c)$  is a function tabulated by Kim [12]. The brightness of a bending magnet source increases linearly with the electron current and with the square of the electron energy. Second generation synchrotrons were designed for fully dedicated operation using an array of bending magnets. Figure 5.1.2 shows the brightness of selected bending magnet sources.

With the invention of insertion devices another important increase was achieved in the beam brilliance. These insertion devices are special magnet arrays inserted into the straight sections between bending magnets. The X-ray spectrum of a wiggler type insertion device with an array of  $N$  pairs of magnets has  $N$  times higher flux than a bending magnet with the same magnetic field. Typical wigglers have  $N=20-50$  with magnetic period of 5 to 15 cm [13].

Undulators are periodic, low magnetic field insertion devices with a peaked X-ray spectrum that is highly collimated in both, vertical and horizontal directions. The spectrum has lower mean energy than for bending magnets or wigglers, but with harmonic peaks of greatly enhanced brightness.

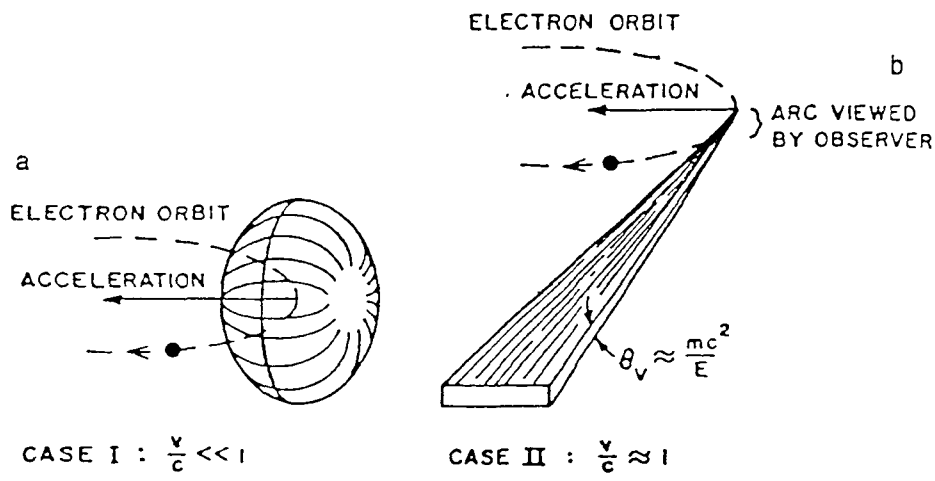


Figure 5.1.1. a) Radiation pattern of electron in circular motion b) Radiation pattern of relativistic electron.

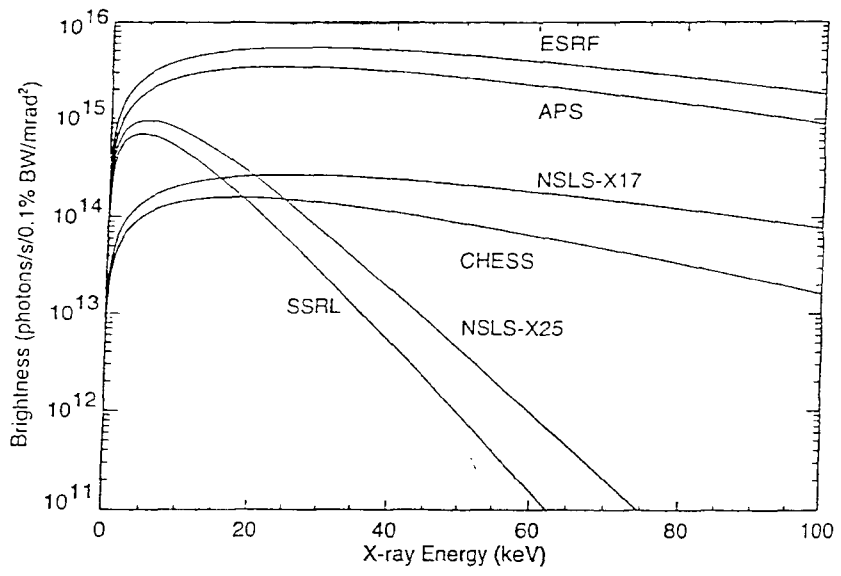


Figure 5.1.2. Brightness from bending magnet sources (reprinted from ANL/APS-TM-3, 1988, with kind permission of Argonne National Laboratory)

### 5.1.3. X-ray microscopes

X-rays striking the atoms of a mineral sample will remove some electrons from their bound state. The excited atoms will regain equilibrium by emitting X-rays (XRF) or Auger electrons. The energy of the photons emitted depends on the quantum number of the initial and final electronic state and the atomic number of the atom. Analysis of these X-ray photons provides information on the abundance of a specific element. The analysis of trace elements with microscopic spatial resolution requires an X-ray source characterized by a very high brilliance.

In general, instruments utilising XRF to obtain two-dimensional maps of element distribution with microscopic resolution are called X-ray microscopes (XRM). The state of the art of XRM was reviewed in an inclusive book chapter by Jones [14]. The primary requirement for an XRM is a micron-size beam of SR. Figure 5.1.3 presents the scheme of a comprehensive XRM beam line using a beam collimated with the use of a pinhole. The sample stage has three-dimensional translation controlled by stepping motors that enables to scan the sample and position the area under analysis into the focus of the optical microscope. Often the entire setup is mounted on a lift table which can be adjusted for precise vertical position. The specimen position is monitored by an optical light microscope that is equipped with a TV camera. The magnification of the objective lens has to fit to an acceptable working distance to avoid interception of the incoming or outgoing beams. A highly effective XRM can be made by using a white beam of X-rays generated by the bending magnet. This approach has been followed by the groups at Hamburg and NSLS [16, 17]. The use of high-intensity white radiation is advantageous for multi-elemental analysis. The photon flux at NSLS for collimated white light is about  $3 \times 10^8$  photons/( $\mu\text{m}^2$ ) for 100 mA of stored electron beam. Collimation is made with a set of four tantalum strips spaced with thin plastic or metal foils to produce a spatial resolution of about 1–2  $\mu\text{m}$  [18]. For optimum operation of collimated XRM the shaping of the incident beam and detected spectrum using filters is mandatory [16].

In the XRM design, the change of polarization as a function of the vertical distance from the electron orbit in the storage ring has to be taken into consideration. The optimal alignment is within a few hundred micrometers of the energy-dispersive detector in the horizontal plane and this condition gives the lowest intensity of scattered radiation [19].

XRM based on focusing X-rays has been of great interest to obtain higher photon fluxes and to improve spatial resolution. Focusing of energetic photons is difficult because of the short absorption depth and the refraction index being less than unity. The focusing itself is based on refractors that have bent shapes and usually result in more or less monochromatic beams. In the equipment used at LURE the beam is incident on a curved crystal of pyrolytic graphite [20]. The commonly used pyrolytic graphite is a mosaic crystal with a spread of  $0.4^\circ$  with about 3% bandwidth at 10 keV. An incident beam of  $2 \times 1$  cm is focused to  $1 \times 1$  mm at an energy of 14 keV.

Scientists from the Free University of Amsterdam constructed a focusing device at Daresbury (SERC) with bent silicon crystals [21]. The scheme of the beam line is presented in Figure 5.1.4.

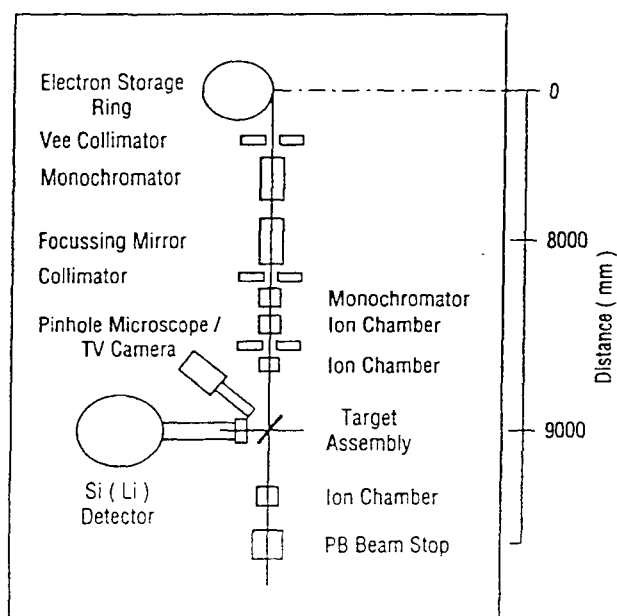


Figure 5.1.3. Scheme of a comprehensive synchrotron XRM beam line. Ion chambers monitor the incoming and transmitted beam intensity and position is viewed by the optical microscope

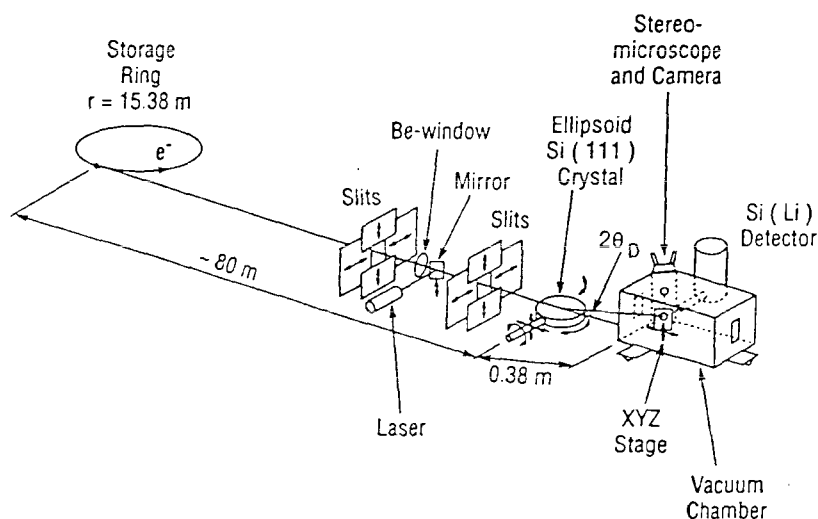


Figure 5.1.4. Scheme of the Daresbury focusing XRM (reprinted from Nucl. Instrum. Meth. Phys. Res., A257, Van Langevelde, p 438, with kind permission of Elsevier Science).

Table 5.1.2  
Characteristics of SR microprobes

Storage ring	Excitation energy (keV)	Beam optics	Spatial size	Photon intensity (ph/s/100 mA)
DORIS	10-20 ( $\Delta E=0.44-1.7$ )	Graphite monochromator	10 $\mu$ m	
NLSL (X-26A)	4-30	Crossed slits	2 $\times$ 2 $\mu$ m <sup>2</sup>	1.8 $\times$ 10 <sup>8</sup> / $\mu$ m <sup>2</sup> ("white")
NLSL (X-26C)	6-14 ( $\Delta E/E=10\%$ )	Kirkpatrick-Baez multilayer (LBL)	6 $\times$ 6 $\mu$ m <sup>2</sup>	5 $\times$ 10 <sup>7</sup> / $\mu$ m <sup>2</sup>
PF (BL4A)	$\leq 10$	Wolter	1.6 $\times$ 34 $\mu$ m <sup>2</sup>	4 $\times$ 10 <sup>6</sup> (8keV) 8 $\times$ 10 <sup>8</sup> ("white")
PF (BL4A)	$\leq 12$	Si(111) monochromator, ellipsoidal mirror	200 $\mu$ m	1 $\times$ 10 <sup>9</sup> (10keV) 2 $\times$ 10 <sup>9</sup> (8keV)
PF (BL4A)		Zone plate (50 $\mu$ m thick)	$\sim$ 3 $\times$ 10 $\mu$ m <sup>2</sup>	2 $\times$ 10 <sup>4</sup> (8keV)
PF (BLSC)	6.2	Si(111) monochromator ellipsoidal Kirkpatrick-Baez	4.2 $\times$ 5.5 $\mu$ m <sup>2</sup>	
SRS	15	Ellipsoidal Si(111)	10 $\times$ 20 $\mu$ m <sup>2</sup> 15 $\mu$ m	10 <sup>6</sup> / $\mu$ m <sup>2</sup> 10 <sup>9</sup>
VEPP-3	4-40	Graphite monochromator	60 $\mu$ m 30 $\mu$ m	(monochromator) ("white")
APS	4-30		0.3 $\mu$ m	10 <sup>10</sup>

The crystal is bent with 100 mm radius in the sagittal plane and 5740 mm in the meridional plane and the photon flux is increased more than 10<sup>4</sup>-fold.

Even more sophisticated schemes have been developed for focusing hard X-rays. Double elliptical mirror (Kirkpatrick-Baez) geometry was designed by the Lawrence Berkeley Laboratory that uses parallel beams of photons to produce an image that is demagnified by about a factor of 100 to produce final images of a few micrometers [22, 23]. The mirrors used are multilayers of tungsten carbide that gives a quasi-monochromatic beam in the sample plane. Most recent developments are Fresnel zone plates [24] and tapered glass capillaries [25]. The characteristics of contemporary SR microprobes are summarized in Table 5.1.2.

#### 5.1.4. Sensitivity and minimum detection limits for XRF

Sensitivity of XRF techniques basically depends on the photoelectric cross section. Radiations and particles used to excite photoelectric emission have different interactions with matter, resulting in different sensitivities for trace element analysis. Figure 5.1.5 presents fluorescence cross sections for typical electron microprobe energy range, proton energy and X-ray tube energies. For photon excitation the fluorescence cross section generally increases with atomic number, but for charged particles it decreases. The maximum cross section for X-ray emission is obtained when the photon energy just exceeds the binding energy of the core electron.

Charged particle excitations, commonly using proton or deuteron beams, have higher ionization cross sections but deposit a few orders of magnitude more energy than photons. On the other hand, for micro-volume analysis, the focusing of charged particle beams is more straightforward and in the last 15 years a big effort was devoted to develop focusing systems for X-rays and charged particles. The lower penetration of the proton beam helps reducing the excited volume of analysis and blurring is less pronounced in a bulk sample where elemental distribution is measured. A number of papers were published in the past decade that compare performance of SRIXE and PIXE [26-29]. For trace element analysis in minerals, the sensitivity for small beam (<10  $\mu\text{m}$ ) analysis should be considered as figure of merit. In order to avoid pileup of major component absorbers on detectors are mandatory. Sensitivity (counts/time/concentration) can be calculated from the expected counting rate of a given element. If the spectrum of the SR beam is known the counting rate of a particular element in a thin sample is given by:

$$I_z = N_A \varepsilon_z d \frac{\Omega}{4\pi} \exp(-\mu_{\text{Al}}(E_z) \chi_{\text{Al}}) \sum_{E_a}^{\infty} I(E) \exp(-\mu_a(E) \chi_a) \sigma_{\text{fl}}(E) dE \quad (5.1.3)$$

where  $I_z$  is the count rate for characteristic peak of atom  $z$  with energy  $E_z$  and  $N_A$  number of atoms in the beam spot,  $\varepsilon_z$  is the detector efficiency for energy  $E_z$ ,  $d\Omega/4\pi$  the solid angle,  $I(E)$  the photon flux of SR beam for energy  $E$  [number of photons/(s  $\text{mm}^2$  0.1 keV bandwidth)],  $\mu_{\text{Al}}(E)$  the linear attenuation coefficient and  $\chi_{\text{Al}}$  the thickness of Al absorber on the detector,  $\mu_a(E)$  and  $\chi_a$  the corresponding values for polyimid absorber,  $\sigma_{\text{fl}}(E)$  the fluorescence cross section of element  $z$  for energy  $E$  and  $E_a$  is the absorption edge energy of the same element. Figure 5.1.6 shows typical sensitivity curves for the BNL XRM.

The limit of detection depends on the peak to background ratio and this figure of merit, in addition to the inherent high brilliance of SR, is very advantageous due to the high polarization factor. X-rays from SR bending magnets are highly polarized with the electric vector in the plane of the electron orbit. For this reason the background spectrum can be minimized if the beam line is properly aligned. Since the electrons roll slightly around the ideal orbit, the polarization is not perfect. In the proper center of the beam the polarization factor can reach 99% but falls off to about 90% at a vertical displacement of one millimeter at a few meters from the front end [14]. Results of the experimental background-to-peak ratio are presented in Figure 5.1.7 where the ratio is presented as a function of displacement. It is important to notice from the figure that displacement becomes more critical for higher atomic number characteristic lines. Proper optimization of alignment for energy dispersive detection is therefore critical [19]. The minimum detection limits (MDL) for zero displacement are shown for the same beam line for microprobe trace analysis in Figure 5.1.8. Considering a sample size equivalent to the smallest excited volume, absolute MDL in the fg range can be obtained [30, 31].

Janssens and coworkers compared the use of X-rays to charge particle microprobes [29]. The study involved NIST glass microsphere standards and the authors found that the collimated XRM and the electron microprobe are the most appropriate instruments for analysis of large number of individual small particles. For mineral applications analytical figures of merit are presented in Table 5.1.3

Recent summaries of synchrotron work [32, 33] give further examples of the SRIXE approach to analysis of geological and environmental specimens.

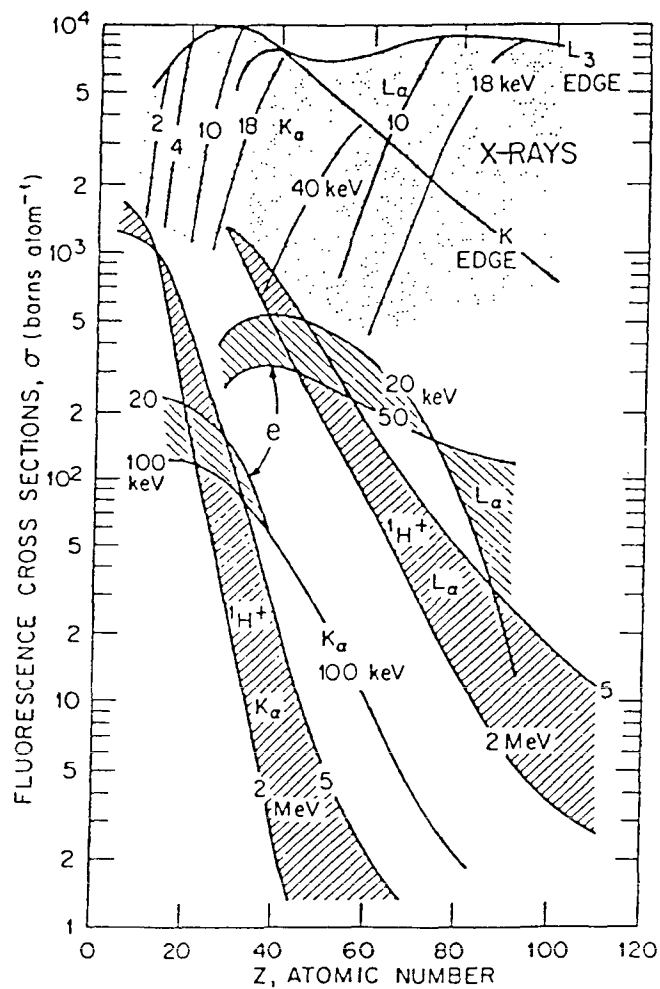


Figure 5.1.5. Dependence of X-ray fluorescence cross sections for electrons, protons, and X-rays on atomic number

Table 5.1.3  
Analytical performance of various microanalytical techniques

	Destruction	Spot size ( $\mu\text{m}$ )	Penetration depth ( $\mu\text{m}$ )	MDL ppm
SIMS	yes	<1	0.01	<1
LAMMA	yes	~1	1	~1
$\mu$ -PIXE	y/n	0.3	5-100	5-10
EPMA	no	<0.1	1-5	>100
XRM	no	3-15	10-100	1-100

### 5.1.5. Applications of XRM

The synchrotron based XRM is being applied in geology and environmental sciences. These applications, either spot analysis of single particles or elemental scans on thin sections or polished specimens, have been reviewed recently by several groups [34-36]. Application are so numerous that here only some examples will be reported.

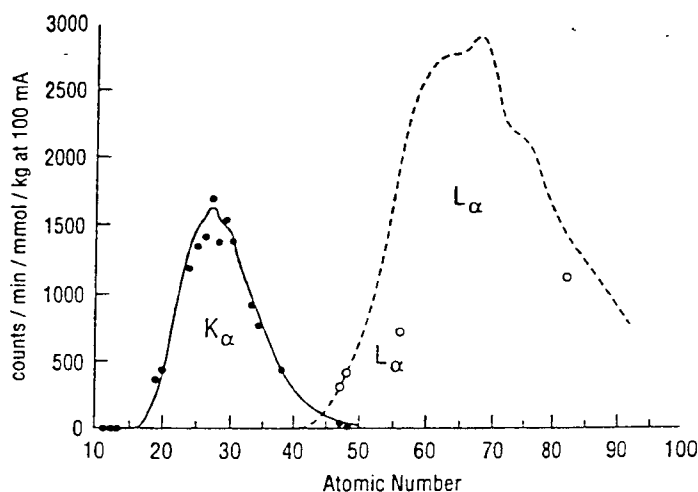


Figure 5.1.6. Sensitivity of the BNL collimated XRM as a function of atomic number for K and L X-ray lines. Measurement conditions are 100 mA storage ring current, 300 counting time, pinhole  $8 \times 8 \mu\text{m}$ , Si(Li) detector 3 mm diameter (reprinted from Nucl. Instrum. Meth. Phys. Res. B50, Kwiatek, p351. 1990, with kind permission of Elsevier Science).

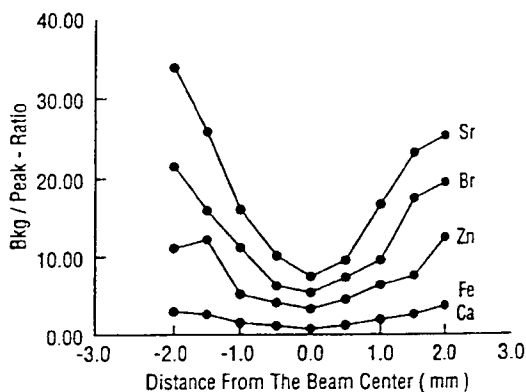


Figure 5.1.7. Experimental results of background to peak ratio as a function of displacement of the detector normal to the plane of the storage ring orbit. The different elements were added to thin gelatin matrix.

It is known that volcanic activity may inject volatile and particulate material to the atmosphere thus influencing the climate. Fine particles can change the balance between atmospheric absorption of incoming solar radiation and outgoing energy. A French group reported on the analysis of aerosols taken from the plume of Mount Etna [37]. Volcanism may inject higher abundances of metals into the Earth's atmosphere than previously suspected. Condensed fumarolic gases escaping from the vent were also studied after condensation onto silica tube. Sixteen elements were determined from the dissolved samples.

Stratospheric dust particles from micrometeorites with ng mass have similar composition to carbonaceous meteorites but are enriched in volatile trace elements [38]. Such particles have microscopic sample volumes and require trace element analysis by XRM. Ablating extraterrestrial objects such as micro meteorites contribute to the stratospheric halogen input destroying the ozone layer. Previous estimates of the input were calculated using average composition of macroscopic meteorites. The analysis of micro meteorites indicates that volatile enrichment compared to conventional meteorites is 40-fold in bromine [39].

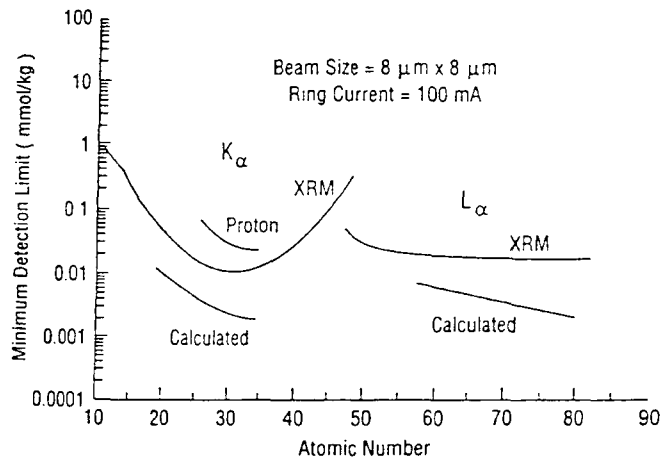


Figure 5.1.8. Measured and calculated MDL for microprobe analysis with same condition as of Figure 5.1.7.

Elemental scans are extremely valuable tools in geochemistry. Element partitioning and chemical migration can be studied with XRM in greater detail than ever. Ores for gold exploration with bulk concentration of 1–10 ppm are economically important, but for developing extraction techniques chemical/mineralogical microanalysis has to be involved. Analysis with XRM demonstrated that pyrite crystals in Carlin-type ores contain little Au compared to the matrix material [40]. With subsequent SEM analysis identification of Au associated with clay mineral illite was possible.

XRM was a useful tool in the study of the evolution of fluids in the coal-forming environment. Sulfur minerals are the reason for high  $\text{SO}_x$  emission of fossil fuel burning.

Sulfides are likely sources of some toxic elements like arsenic and lead. Pyrite, marcasite and coprocyrite in British coal deposits was analyzed for toxic elements. Coal overlying a marine bed contained high levels of toxic metals in the pyrite inclusions [41].

## 5.2. ION BEAM ANALYSIS

### Introduction

The analytical applications of the intense X-ray beams produced at synchrotron storage rings are complemented and extended by the use of MeV-energy ion beams. The technologies for production and focusing of ion beams have been developed over a period of more than 60 years. As a result, beams can be produced with diameters of less than 1  $\mu\text{m}$  and with flux values up to  $10^{11}$  ions/ $\mu\text{m}^2$  [42]. Ion beams lose energy by ionization of the atoms composing the stopping material caused by the interaction of the Coulomb field of the projectile with the atomic electrons and also by nuclear scattering from the nuclei of the atoms. The range of ion beams in materials is short, with a relatively well defined end point. By comparison, X-ray beams are attenuated according to an exponential law and sample a much greater amount of material.

Ion beams can be used for trace element determinations using the characteristic X-rays produced in the ionization process (PIXE). Ion beams can also interact directly with atomic nuclei. Elastic scattering of the nuclei can be used to identify the masses of atoms present in the sample. Nuclear reactions, including elastic and inelastic scattering or Coulomb excitation, can be used to identify specific elements and nuclides present in the sample. The sensitivities for detection of the light elements (below Ca or so) is particularly good compared to PIXE. This is because the X-ray fluorescence yield decreases strongly with atomic number. Thus, use of inelastic scattering permits detection of elements such as lithium, boron, and fluorine, which are difficult to detect with XRF.

Detection methods for X-rays,  $\gamma$  rays, charged particles and neutrons have been developed in parallel with the development of accelerators, ion sources and other instruments necessary for the production of ion beams. This work has been driven by the need for basic understanding of nuclear physics, by practical considerations related to nuclear power and nuclear weapons development, medical applications, etc. Many of the analytical uses of ion beams have also stemmed from the applicability of these methods to study semiconductor materials used for production of various types of electronic devices.

The uses of ion beam analysis (IBA) to study geological materials have been developed intensively over the same period. Our intent is to summarize the experimental approach and describe briefly several experiments that show how ion beams are applied and how the analytical approach complements the results from application of synchrotron beams. For example, measurements of diffusion, fluid inclusions, macerals in coal, and invisible gold can be made using both synchrotron radiation or ion beam analysis. Kucha et al. [43] studied accumulations of Au and Pt group elements in black shale and organic matrix produced in a Polish mine using electron microprobe, microbeam PIXE, synchrotron microprobe and transmission electron microscopy. Inclusions have been investigated using ion beams [44–46] and X-rays [47]. Practical performance for the ion and X-ray microprobes are rather similar at the present time although applications can make plausible cases demonstrating the superiority of one or the other approaches.

Combination of the PIXE method with nuclear reaction analysis, activation analysis, and elastic recoil detection gives a diverse suite of techniques which can be used to determine elemental compositions for elements from hydrogen to the transuranic elements.

There is a large literature on the subject of elemental analysis using ion beams and on the application of the technique to the analysis of geological materials. A representative selection of material is given here so that the newcomer to the field can easily locate some of the basic literature. The papers by Campbell [48] and Sie et al. [49] survey some of the applications in geology. Useful overall views related to the field of ion beam analysis are provided by several authors [50–57]. There have also been a series of conferences on microbeam analysis which permit a rapid overview of the state of nuclear microprobe technology and applications in geological, environmental, and other sciences at many different laboratories [58–60].

### 5.2.1. Nuclear and x-ray data sources

Application of ion beam (and photon beam) analysis rests on an enormous body of knowledge gained in experiments carried over a time period covering the entire 20th century. Some of the topics of interest include nuclear reaction Q-values which represent the energy released in a nuclear reaction, ranges and energy loss mechanisms for ion beams stopping in different materials, cross sections for X-ray production, and cross sections for nuclear reactions.

The National Nuclear Data Center at Brookhaven National Laboratory is a valuable resource for obtaining summary data for many types of nuclear and atomic cross section data. Access is available through the Internet [61]. An exhaustive listing of particle ranges and stopping powers have been produced by Northcliffe and Schilling [62], Andersen and Ziegler [63], and Ziegler and Chu [64] as well as many other authors. Ziegler has also made available a computer program, TRIM, for calculation of ranges and other parameters of interest [65]. Tapper et al. [66] give a useful overview of PIXE which includes helpful references for many of the physical parameters needed for application of ion beam analysis.

### 5.2.2. Accelerator facilities

Accelerators used for analysis of materials are, for the most part, either single-ended or tandem type van de Graaff accelerators. Very often these are machines which were originally constructed for nuclear physics research and have been turned to other uses as the effort in low-energy nuclear physics decayed away. On the other hand, the field has grown to such an extent that machines designed specifically for analytical applications now exist. Descriptions of the accelerators and the ancillary equipment used at a few of these locations are given for Bochum [42], for Heidelberg [67], for Oxford [68]; for the machine in Los Alamos [69, 70], for Australia [71], for Lund [72]; for South-Africa [73], and for Saclay [74]. A general review has been given by the Oxford group [75].

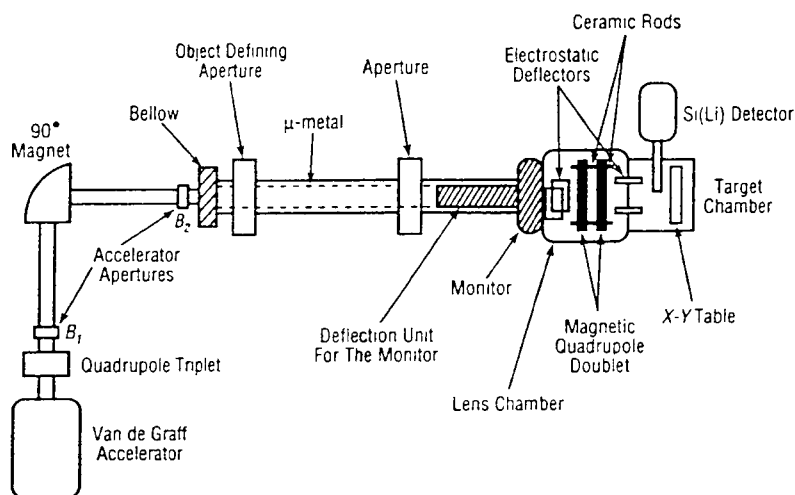


Figure 5.2.1. Diagram of the principal components of the Heidelberg proton microprobe system (From Bohsung et al., 1995)

The Heidelberg proton microprobe serves as a good example of an ion microprobe laboratory. Work at Heidelberg has been going on for more than 20 years in this area [76]. This illustrates the need for long-term dedication to the development and refinement of the analytical procedures employed in ion beam analysis that provide the foundation for doing refined characterization of geological and other materials. The Heidelberg facility is based on a single-ended 3 MeV van de Graaff accelerator. A diagram of the apparatus is shown in Figure 5.2.1. The high performance of the system is obtained by meticulous attention to the design and fabrication of the collimation apertures and focusing system (quadrupole doublet). Beam sizes of  $<1 \mu\text{m}$  are obtained at beam energies of 2–2.5 MeV and currents of 15–500 pA. Typical PIXE spectra obtained with the Heidelberg microprobe are shown in Figure 5.2.2.

### 5.2.3. Nuclear reaction analysis

Nuclear reactions can be used to make sensitive determinations of many specific isotopes. In general, nuclear reactions and elastic scattering can be used for detection of specific elements/isotopes throughout the periodic table. However, nuclear reaction analysis is particularly helpful for elements with  $Z < 20$  since sensitivity of X-ray measurements decreases sharply for smaller atomic numbers. In addition, the Coulomb barrier increases with atomic number so that the reaction cross sections will drop for the particle energies produced by many of the van de Graaff accelerators used for this type of measurement. The magnitude of the cross sections are generally of the order of tens of mb. As a result, detection limits generally will not approach trace element concentrations for beam sizes of the order of micrometers.

#### *Hydrogen detection*

Hydrogen can be detected by using nuclear reactions or by elastic scattering. Both approaches can be used to find the total amount of hydrogen contained in the volume probed by the beam and the distribution of hydrogen as a function of depth below the sample surface.

Two nuclear reactions are commonly used:  ${}^1\text{H}({}^{15}\text{N}, \alpha\gamma){}^{12}\text{C}$  and  ${}^1\text{H}({}^{19}\text{F}, \alpha\gamma){}^{16}\text{O}$ . The energies of the emitted gamma rays are 4.4 MeV and 6.13 MeV, respectively. Both reactions are strongly resonant. Adjustment of the incident ion energy places the resonant energy at various points below the surface so that the H depth profile can be measured. The depth resolution is around 10 nm at the surface but decreases to a value of about 35 nm at a depth of 1 mm because of energy straggling caused by the beam stopping process. Detection limits for hydrogen are about 0.1 wt. %.

Use of a tandem van de Graaff type of accelerator is convenient for this reason. The usefulness of this method is reduced by two factors: 1) the high sample damage caused by the heavy ion beams and 2) the relatively poor detection limits achieved.

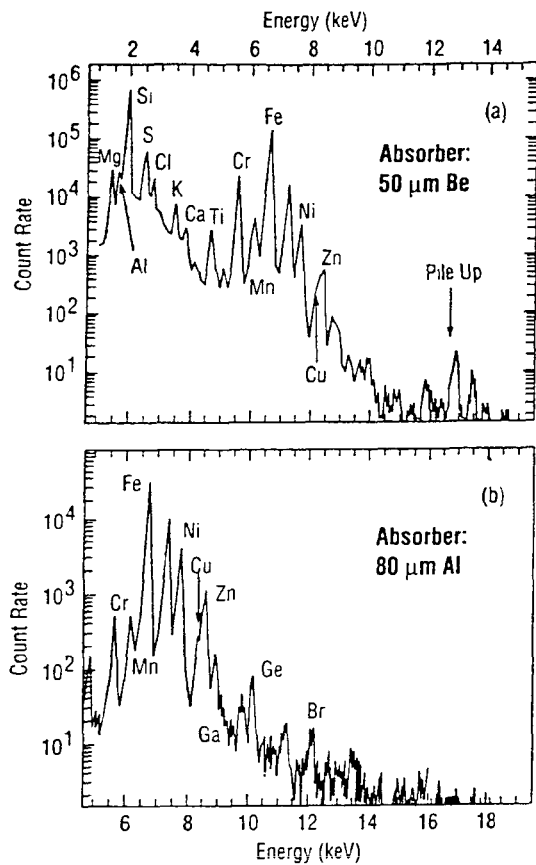


Figure 5.2.2. Typical X-ray spectra obtained from a single interplanetary dust particle. Beryllium and aluminum absorbers are used to shape the spectra for optimal detection of light and heavy elements, respectively. (From Bohsung et al., 1995.)

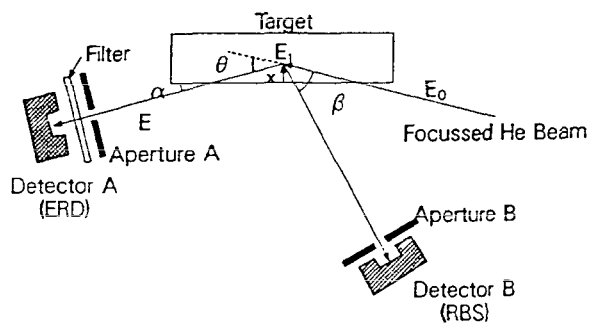


Figure 5.2.3. ERD experimental approach. (From Hu et al., 1990.)

Toulhoat et al. [77] have also demonstrated the feasibility of using tritons produced in the  ${}^2\text{H}(d,p){}^3\text{H}$  reaction for determination of deuterium. They analysed a sandstone and found evidence that deuterium was abundant at grain boundaries and on particle surfaces.

An alternate approach is based on elastic scattering of protons. If thin samples can be prepared, it is convenient to measure the scattered ions at  $45^\circ$  to the incident beam with detectors placed on either side of the beam. Coincidence techniques are used to reduce background produced by scattering from heavier elements. The hydrogen concentration as a function of depth below the surface of the sample is obtained by measuring the energy of the scattered protons.

The elastic scattering of alpha particles by target hydrogen nuclei is also effective. This is the elastic recoil detection (ERD) approach [78]. ERD relies on differences in the ranges of protons and helium to make possible an effective separation between incident and scattered particles. A diagram showing the experimental approach is given in Figure 5.2.3. The most important parameter for ERD studies is the cross section for  $\text{H}(\text{He},\text{He})\text{H}$  scattering. The first detailed study was that of Critchfield and Dodder [79]. The current cross section values have been reviewed recently [80, 81]. (Note that the nearly fifty-year span during basic nuclear physics work was carried out and finally applied to hydrogen determination in geological materials. This illustrates how long it took to accumulate the great mass of ion beam data and techniques that underlies the analytical application of ion beam techniques and to finally apply them to study of geological materials.)

Hu et al. [78] applied the ERD method to the measurement of hydrogen in phlogopite and olivine in a peridotite specimen. The spectra of recoil protons produced in the bombardment of a polyimide calibration foil, phlogopite, and olivine with a 2.5 MeV helium beam with a diameter of  $30\ \mu\text{m}$  are shown in Figure 5.2.4. The peak at the high energy end of the spectrum comes from an enhancement of hydrogen at the surface. Bulk concentrations were estimated from the region shown in the interior of the specimen. Hydrogen concentrations of 0.40 and 0.087 wt.% were found for phlogopite and olivine, respectively. Sie et al. [81] looked at two artificial specimens composed of anorthite and diopside prepared with different concentrations of hydrogen with a similar experimental arrangement. They estimated a minimum detection limit for hydrogen of about 10 ppm for an integrated beam charge of  $0.3\ \mu\text{C}$ .

#### *Other applications of NRA*

Many different reactions are available for NRA. The  $(p,p'\gamma)$  reaction can be used for detection of Li, B, F, Na, Mg, and Al. Detection of gamma rays with a germanium detector is easy and permits the use of thick (compared to the proton range) or thin targets placed in very simple target chambers. Alternatively, charged particles from the nuclear reactions can be detected using surface barrier detectors or neutrons using several different types of detectors. In this case, target thicknesses need to be kept small so as not to introduce a broadening in the energy of the emitted particles large enough to make it difficult to resolve individual peaks. Other types of reactions that have been used for geological studies include  $(p,p')$ ,  $(p,n)$ ,  $(p,\alpha)$ ,  $(d,p)$ , and  $(d,\alpha)$  reactions. The product heavy nucleus produced in the reaction is sometimes radioactive with a relatively short (minutes or less) half life. A measurement of the decay of the residual activity then gives the isotope producing the radiation and the concentration of the target atoms in the sample.

Toulhoat et al. [82] have discussed the use of nuclear reactions for detection of deuterium, nitrogen, and carbon in oil field rocks (oolitic carbonate and sandstone) and lithium and boron in phyllosilicate, pyroxene, and tourmaline. Their work included an investigation of the stability of the materials under proton bombardment, determination of detection limits, for the various reactions studied, and extraction of the isotopic ratios for lithium and boron. Figure 5.2.5 shows the variation of D, C, and O in a scan over two grains of a sandstone and demonstrates the ability of the nuclear reaction technique to obtain the significant information on the spatial distribution of the materials in reservoir rocks and hence to obtain a better understanding of interactions between the oil and mineral surfaces that may influence oil recovery. Mercier et al. [83] have carried on a further confirming investigation with a variety of nuclear reactions and PIXE using samples prepared in the laboratory from Fontainebleau sandstones and silica pellets.

Other experiments have been carried out to determine the nitrogen content of upper mantle and peralkaline magmatic micas [84] and of feldspar, biotite, and muscovite crystals taken from shales found in Morocco [85]. Sutton et al. [84] used the  $(d,\alpha)$  reaction with a microbeam of  $50\ \mu\text{m}$  produced by an electrostatic quadrupole double lens while Mosbah et al. [85] relied on the  $(d,p)$

reaction and a  $15 \times 15 \mu\text{m}^2$  beam formed with a magnetic quadruple triplet lens. Minimum detection limits were about 5 ppm for the experiment of Sutton et al. and about 50 ppm for the work of Mosbah et al. Results found for the upper mantle and peralkaline magmatic micas examined by Sutton et al. are given in Table 5.2.1. An interesting bimodal distribution of nitrogen concentrations was found pointing to different concentration processes. Mosbah et al. found high N concentrations in pegmatite (roughly 450 ppm) and even higher concentrations in micaschist (roughly  $1900 \text{ ppm} \pm 500 \text{ ppm}$ ). Mosbah et al. also found reasonable agreement with bulk measurements of N content found using catharometry and Fourier transform infrared spectroscopy. The nuclear reaction method has better detection limits in addition to its superior spatial resolution.

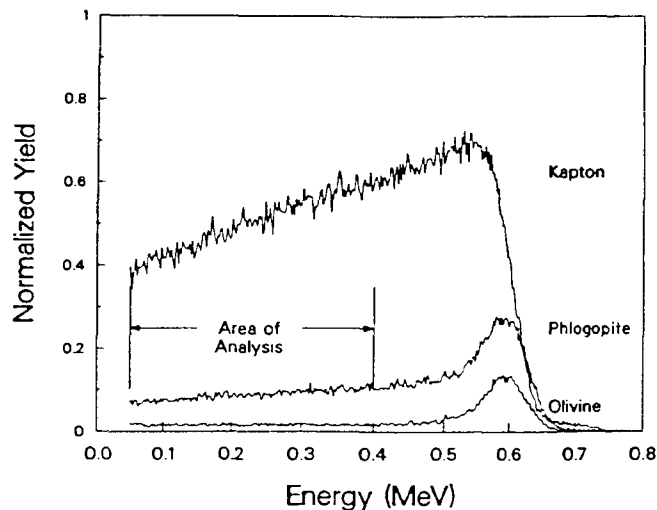


Figure 5.2.4. The spectra of recoil protons produced in the bombardment of a polyimide calibration foil, phlogopite, and olivine with a 2.5 MeV helium beam with a diameter of  $30 \mu\text{m}$  are shown (Hu et al., 1990).

Table 5.2.1  
Summary of nitrogen concentrations obtained for upper mantle and prealkaline magmatic micas using the  $^{14}\text{N}(d,\alpha)^{12}\text{C}$  reaction

Specimen description	Location	Content (ppm) <sup>a</sup>
<b>Kimberlites</b>		
BD 1380 Megacryst	Monastery, S. Africa	$8 \pm 4$
BD 1823 Megacryst	Excelsior, S. Africa	$4 \pm 4$
BD 1083 Megacryst	Wesselton, S. Africa	$7 \pm 4$
BD 1118 Megacryst	Jagersfontein, S. Africa	$21 \pm 4$
<b>Carbonatites</b>		
BD 35 Microjollite megacryst	Oldoinyo Lengai, Tanzania	$14 \pm 6$
BD 82 Nepheline syenite megacryst	Oldoinyo Lengai, Tanzania	$19 \pm 7$
<b>MARID and Glimmerites</b>		
BD 1165 Pyroxene glimmerite	Roberts Victor, S. Africa	$85 \pm 20$
BD 3089 MARID diopside-rich	Bultfontein, S. Africa	$90 \pm 16$
BD 1158 Ilmenite glimmerite	Bultfontein, S. Africa	$210 \pm 33$
BD 1159 Amphibole glimmerite	Bultfontein, S. Africa	$240 \pm 40$

<sup>a</sup> Uncertainties are 1 standard deviation counting statistics.

Table 5.2.2  
Fluorine content in Polish clays following firing  
at 1200 °C for 2 h. (Wyszomirski and Urban, 1992)

Deposit	F[ppm]
Bonarka, Kraków	<DL
Grójec	<DL
Jakubów	<DL
Kozłowa Góra	<DL
Leknica	<DL
Mikolów	<DL
Slawków	<DL
Stara Góra	<DL
Turów II	<DL
Wola Rzedzanska	170
Zebrydowa	200
Zebrydowa	250
Zeskawice, Kraków	<DL
Zielinki, Kraków	100
Zamów	<DL

Fluorine concentrations in materials are readily found by observation of the 110 and 197 keV  $\gamma$ -rays produced in the (p,p' $\gamma$ ) reaction. Przybyšowicz et al. [86] measured the fluorine content of bulk samples of serpentinite rocks found in south-west Poland. A gamma ray spectrum found from bombardment of these rocks is shown in Figure 5.2.6. Note that there is multi-elemental sensitivity so that F, Na, Mg, and Al can be measured simultaneously. The experiment found that the average fluorine content in the serpentinites is about 200 ppm and that there was no dependence on the degree of alteration of the initial peridotite into serpentinite. Another experiment performed at

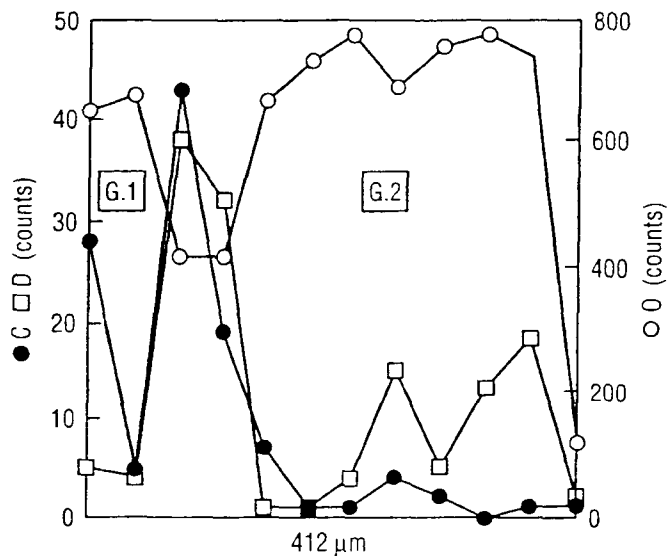


Figure 5.2.5. Line scan across two grains in sandstone showing an enhancement of deuterium and carbon at the boundary between the grains (Touhoat et al., 1991)

Kraków [87] studied the emission of fluorine during firing of Polish clays. In this case measurements of the fluorine content before and after firing made it possible to estimate the atmospheric release of fluorine during the firing process. The results obtained from examination of a large suite of raw clays is shown in Figure 5.2.7. These values are to be compared with the fluorine contents measured after firing for 2 hours at 1200 °C shown in Table 5.2.2. A total annual emission of around 164,000 kg was estimated for 1990 and was considered comparable to emissions from aluminum, fertilizer, glass, and enamel industries. Ion beam analysis was useful in this case for its high sensitivity and ease of sample preparation compared to other analytical methods.

#### 5.2.4. PIXE Analysis

PIXE is by far the most widely applied of all ion-beam related techniques used in analysis of geological and environmentally related materials. PIXE can be used for the routine detection of elements with atomic numbers greater than perhaps thirteen using simple energy dispersive X-ray detectors. The detection limits are not constant across the periodic table, but are extremely good in many critical regions such as for the transition elements and for heavy elements such as lead and mercury. It can be used in different modes: broad beam for analysis of bulk samples and microbeam for measurement of individual features. Maps of the composition of heterogeneous samples can be obtained by rastering the beam across the sample and making a point-by-point determination of the elements present.

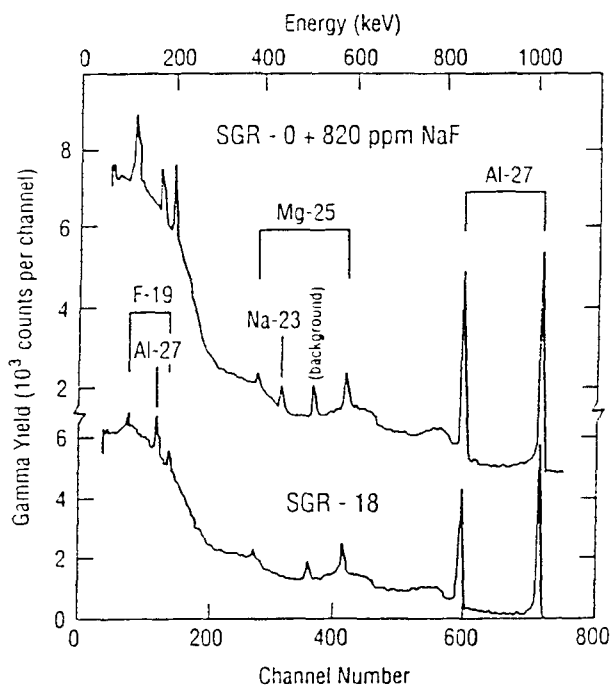


Figure 5.2.6. Gamma-ray spectrum produced by a 10-minute bombardment of serpentinite rocks by a 2.6 MeV 10 nA proton beam. (Przybyłowicz et al., 1986).

### 5.2.5. Applications of IBA in geology

It should be clear that in many cases simultaneous measurements can be made using detection of X-rays (PIXE), proton-induced gamma ray emission (PIGE) and nuclear reaction analysis (NRA), including elastic scattering. The combination of these methods makes it feasible to analyse all elements in the periodic table from hydrogen to uranium.

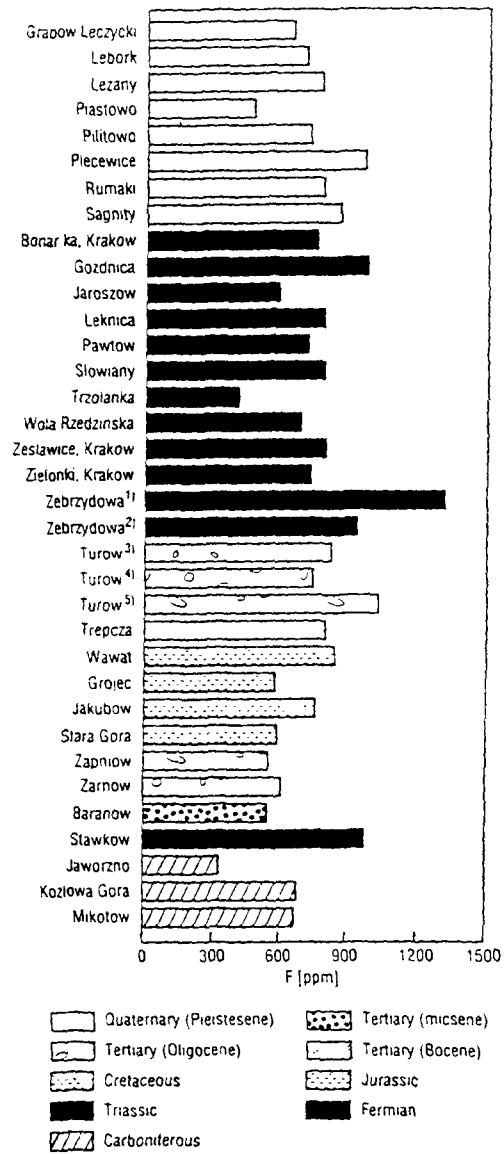


Figure 5.2.7. Fluorine content in clays taken from various sites in Poland. (Wyszomirski and Urban, 1992).

An early example of the combination of analytical methods is given by Carlsson and Akselsson [88]. They used PIXE to cover the range of elements from Al to U and PIGE to determine Li, B, F, Na, Mg, and Al. They made quantitative measurements of elemental concentrations on a number of rock standards obtained from the US Geological Survey and obtained agreement within better than 10% with values found from standard analytical methods. Malmqvist et al. [89] applied this approach to the analysis of drill-core specimens and suggested that the instrumentation could be generally useful for the mining industry.

Vogt et al. [90] report the use of PIXE, PIGE, and proton backscattering combined with electron probe microanalysis for the analysis of mineral grains and isolated minerals. In this case the beam size was defined by a mechanical collimator which could produce beams of variable diameter between 400 and 7000  $\mu\text{m}$ . Figure 5.2.8 shows the results of differentiating and smoothing the energy spectrum of protons elastically scattered by a thick target of clinopyroxene. This shows the ability of the elastic scattering to clearly resolve elements lighter than neon, but with much poorer mass resolution for the heavier elements. Nevertheless, it is clear that the elastic scattering spectrum can yield a great amount of useful information with minimal effort.

PIXE has been a major tool for the analysis of air-filter samples. Annegarn and Przybyšowicz [91] have added additional analytical techniques to these analyses so that chemical mass balance determinations can be made. Beta absorption is used to determine the total mass of the aerosol being measured. Light elements were investigated using PIGE although beam-induced damage to the filters was troublesome. Inorganic carbon could be estimated from optical absorption and the heavier elements from PIXE. The combined system represents a substantial improvement to the analysis of aerosol samples and makes possible the use of the data for chemical mass balance models.

Makjanic et al. [92] report using the (d,p) reaction to localize C and O in various types of chondrites. In addition, PIXE was used to determine the intensities of Si, S, Ca, K, Cr, Ti, Mn, Fe, and Ni. Line scans along the polished surface of chondrite were made using a 100–300 pA beam of 1.4 MeV with a size of  $5 \times 20 \mu\text{m}^2$ . A line scan showing the intensity of O, Fe, S, and C in a Kelly chondrite is given in Figure 5.2.9. The C scan shows a peak consistent with a C film on the surface of the troilite that is defined by the peaks in the Fe and S scans. The authors discuss the problems caused by the use of a thick target and the different depth of material analyzed by the nuclear reaction and PIXE methods.

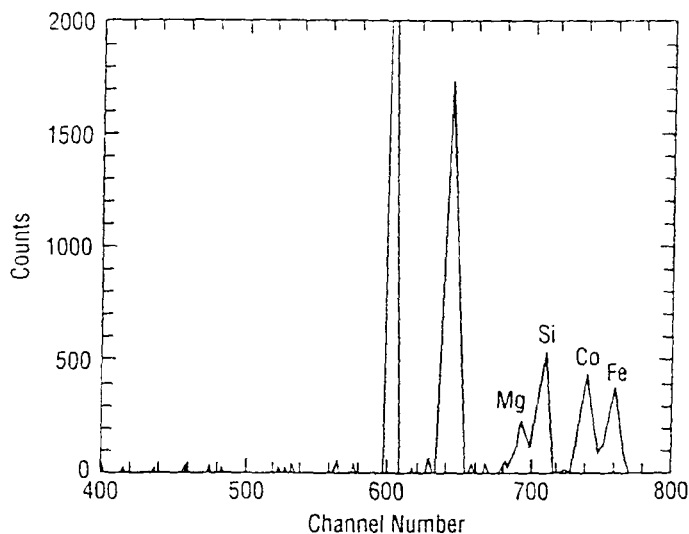


Figure 5.2.8. Rutherford backscattering spectrum for clinopyroxene following numerical differentiation and smoothing. Peak positions for elements from Mg to Fe are clearly defined. (J. Vogt et al., 1992).

### Precious metals

Investigation of ores containing gold, platinum and other precious metals has been actively pursued by many groups because of the economic significance of these elements. In particular, recovery of these elements from the native ore is not efficient and a major amount of the material is not recovered at all. In principle, better knowledge of the micro distribution of the elemental composition of the ore could well bring about better extraction methods and result in direct economic return.

It is also interesting to note the ways in which different analytical techniques have been used in the work. Some of the relevant experiments are presented by a number of recent publications [93-109]. The analytical techniques used include proton induced X-ray emission, synchrotron-radiation induced X-ray emission, accelerator mass-spectrometry, secondary-ion mass spectrometry (ion microprobe), electron probe microanalysis, and transmission electron microscopy. The different ores investigated include the Carlin deposits in Nevada, Zechstein copper deposits in Poland, Kidd Creek mine in Ontario, Wellgreen deposit in the Yukon, Moberly VMS deposit near Rouyn-Norand Quebec, sulfide ores in the Noril'sk-Talnakh district of Siberia, the Freetown layered complex in Sierra Leone, and several locations in Western Australia.

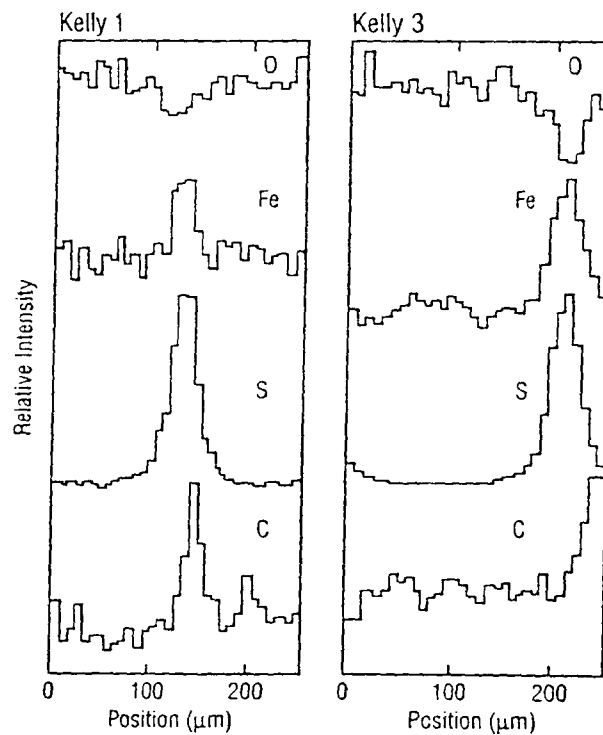


Figure 5.2.9. Distribution of O, Fe, S, and C for two line scans on a Kelly chondrite. The position of the C peak indicates the existence of a carbon-rich layer on the surface of the troilite indicated by the peaks in the Fe and S distribution. (J. Makjanic et al.)

vely  
lar,  
erial  
ntal  
rect

d in  
ions  
ron-  
nass  
tron  
stein  
brun  
eria,

The general problem of precious metal mineralogy is summarized by in a review paper [95]. The distribution of trace amounts of the precious metals in minerals and ores is summarized. The application of microanalytical techniques and their role in better understanding the location of the precious elements is emphasized. The techniques that are mentioned include electron-, proton-, and ion-beam based microprobes. Cabri emphasizes the importance of these methods and also the complementary information each method gives.

An example of a comprehensive study of gold and platinum group elements in the black shale and organic matrix of the Kupferschiefer deposit in Poland is the work of Kucha et al. [43]. This was a multinational collaboration combining groups in Kraków, Heidelberg, and Amsterdam working with instrumentation in Poland, Austria, Germany, and Great Britain. Comparison of measurements made with electron, proton, and synchrotron microprobes are shown and reasons for discrepancies are pointed out. Results for elemental concentrations of many elements in the clay-organic matrix of the shale were found using proton and electron probes. Evidence for the existence of palladium, silver, platinum, and gold in the clay-organic matrix was demonstrated.

### *Fluid inclusions*

Fluid inclusions in rocks are studied to gain insights into the processes by which rock systems are produced, formation of metal deposits, and other related phenomena. Measurement of the trapped fluids in these inclusions is difficult using conventional techniques. The relatively great depths to which X-rays or protons used in SRIXE and PIXE penetrate the rocks makes possible the application of fluorescence techniques to study of the problem. The limitations of fluorescence are defined by the escape depths of the fluorescent X-rays being studied which are of the order of perhaps 10  $\mu\text{m}$  for elements such as Cl, K, and Ca. Preparation of the inclusion samples is therefore a delicate matter and must be able to produce specimens which have an overlying rock layer thin compared to the escape depth. The finite volume of the inclusion also impedes the derivation of accurate concentration values for the trace elements in the inclusion fluids.

An Australian group [43, 110, 111] has carried out a series of investigations of fluid inclusions using PIXE. The aim in this case is to determine the ore metal concentrations as they segregate between magmatic brine and vapor. Ryan et al. [112] discuss the analytical approach to standardless analysis of fluid inclusions. They include the effects of the finite inclusion volume, nonuniform beam intensity profiles, and vapor bubbles. The techniques can produce analyses of 10–15  $\mu\text{m}$  inclusions with uncertainties of about 40% for Cl and 20–30% for heavier elements. Heinrich et al. [45] used this approach to measure elemental concentrations in brine and low-salinity vapor inclusions in granites from the Mole Granite district in Australia. They find partitioning of metals between magmatic vapor and hyper saline brine can be substantial and sulfur complexing may be responsible for partitioning into the magmatic vapor phase while chloride complexing causes partitioning into the brine. Arguments for the importance of these mechanisms in solutions related to ore formation are presented. Heinrich and Ryan [111] use the PIXE data as input to a model that could be used to predict chemical behavior during cooling of the brine. It was concluded that the PIXE measurements confirm that mineralization is a consequence at least in part, of the cooling of metal-bearing magma solutions.

Similar experiments have been done using SRIXE. Frantz et al. [47] measured Ca, Mn, and Zn concentrations in laboratory-prepared inclusions. Measured metal concentrations were found to be in reasonable agreement with the concentrations in the initial fluids. Raster maps of the inclusions show both the shapes of the inclusions and the positions of vapor bubbles. Lowenstern et al. [113] then applied the SRIXE approach to the partitioning of copper into the magmatic vapor phase.

Finally, it is appropriate to point out that the use of synchrotron computed microtomography may well be of great importance in the study of fluid inclusions in the future. In this case, the imaging contrast will be obtained through detection of fluorescent X-rays. The high intensity X-ray fluxes delivered by third generation synchrotron X-ray sources will make the rapid acquisition of tomographic data possible. Volumetric concentration data with micrometer size volume resolution will then give images of not only the fluids, but also of the neighboring rock so that diffusion of the trace elements into the rocks can be determined simultaneously.

ndicates

1.

### *Investigations of coal macerals*

Hickmott and Baldrige [114] have applied PIXE microanalysis to determine the composition of macerals and sulfides from the lower Kittanning coal of Western Pennsylvania. They point out that the results of investigation of coal macerals may help in defining the formation history of the coals beds, in choosing coal-beneficiation methods, and estimating release of toxic elements contained in the coal during the combustion process. As is pointed out by Hickmott and Baldrige, relatively few experiments have been carried out using high-resolution microprobes capable of high-sensitivity multi-elemental detection. Among earlier applications of the PIXE technique include work by Chen et al. [115] and Vajic et al. [116]. Parallel experiments using the synchrotron X-ray microprobe have been performed as well [117-119].

The experiment of Hickmott and Baldrige used a proton microprobe with a spatial resolutions of 5  $\mu\text{m}$  for analysis of sulfide grains and vitrinite macerals, respectively. They found that there was significant trace element heterogeneity within individual sulfide grains and suggest this could result from a complex growth history for the grains. The same behavior was found for the trace elements in the vitrinite macerals. Correlations in trace element compositions were also found for sulfides and vitrinite macerals taken from coals overlain by marine, brackish, or fresh water shale beds. It was suggested that measurements should be done on facies samples taken from well-established locations in the coal seam (see also [119]).

### *Investigations of meteorites*

Meteorites may include complex structures which demand high-spatial resolution, multi-elemental sensitivity, and low minimum detection limits. PIXE clearly fulfills these needs very well. Several relevant experiments have been performed with the Heidelberg microprobe that cast light on the thermal histories of meteorites.

Bajt and Traxel [120] investigated trace element distributions in single olivine crystals found in the Semarkona and Dhajala chondrites. Scans were made to determine the variation of Fe, Mn, Ni, Cr, Ca, Ti, and V were made from the surface of what was taken to be an isolated, relict crystal grown from the vapor phase. Fe, Mn, and Ni were found to reach maximum concentration values at around 100  $\mu\text{m}$  below the surface. The other were maximized at the surface and decreased going into the crystal. The authors classify Ti, Ca, V, and Cr as refractory or semi-refractory elements as compared to Mn, Fe, and Ni which are classified as volatile elements. It is then argued that the volatile elements give information on the latter stages of the crystal cooling process and that the refractory and semi-refractory elements give evidence on the early stages of cooling. A simple model based on a sudden reheating of the crystal was developed to predict the trace element distributions. Reasonable agreement with the experimental values was found. Measurements were also made on olivine crystals contained in the chondrule and results markedly different from the isolated crystal were found in terms of both trace element concentrations and concentration profiles. Further exploitation of this approach should yield valuable new information on formation processes in meteorites.

The above measurements were extended to include copper, zinc, gallium and germanium distributions in taenite lamellae of iron meteorites with a spatial resolution of 2  $\mu\text{m}$  to see if cooling rates of meteorites can be estimated in the temperature range from 400  $^{\circ}\text{C}$  as has been done using nickel [121]. The authors conclude from their analysis of the data that the Cu profile are similar to those for nickel. Little difference is found between the diffusion of Cu in Fe and Ni in iron so that use of copper will not extend the temperature range to be investigated. It was also thought to be unlikely that use of the other elements would be useful for determination of cooling rates.

### *Zoning*

Zoning is a common occurrence in minerals possibly showing the influence of changing conditions during formation. While examples are cited elsewhere it seems worthwhile to explicitly cite several examples of the recent applications of PIXE.

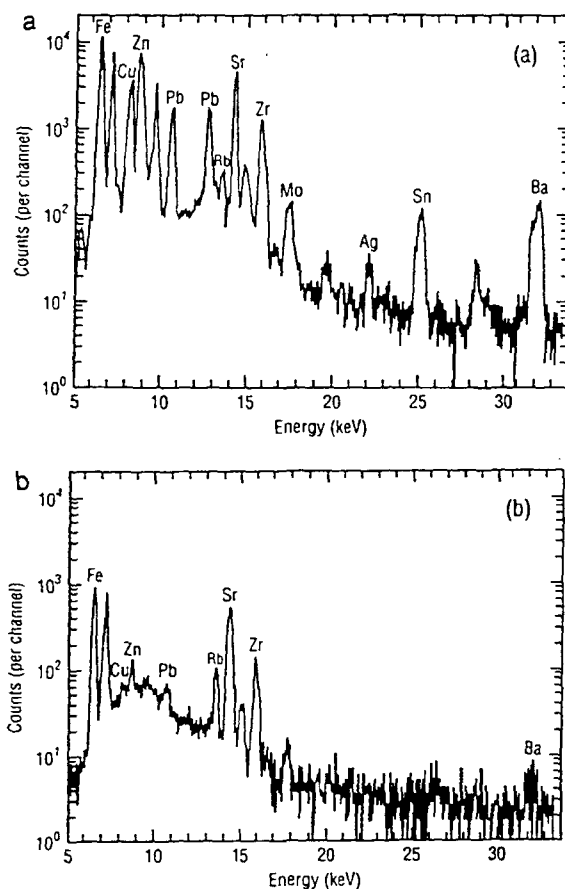


Figure 5.2.10. PIXE spectra obtained for an area close to the worm burrow (a) and in the nearby soil (b) (Protz et al.).

Hickmott and Spear [122] studied major- and trace-element zoning in garnets from Massachusetts using proton-, electron-, and ion-microprobes. They concluded that trace-element zoning can be used to understand reaction histories and it is also suggested that the information would aid in understanding P-T paths.

Teesdale et al. [123] have emphasized the utility of the proton microprobe for making line scans or full area maps of elemental distributions for minor and trace elements that reveal oscillatory zoning in natural and synthetic minerals and for other related applications. Oscillatory zoning was demonstrated in a vesuvianite mineral. A 2-D map showed oscillations in the rare earth element concentrations at the size of 10–30  $\mu\text{m}$  compared to a scale of 50–100  $\mu\text{m}$  Fe, Ba, and Ea. It is speculated that the substitution mechanisms are different for the two cases. Measurements can be made of the adsorption of trace and minor elements at mineral boundaries. This can be done reliable because the scattering of the proton beam is much smaller than the scattering of electron beams used in the electron microprobe. Results of a scan and map of a titanate grain demonstrated that zoning could be observed in the titanium distribution and that several of the trace elements are found outside the edge of the crystal as defined by the titanium distribution. Examples of the zoning of rare earth elements in synthetic calcite and in calcite cements from a lower-Paleozoic limestone. PIXE mapping yields a wealth of information that should be extremely useful in obtaining more refined models for the processes taking place in mineral formation and modification.

### Elemental transport in soils by worms

Protz et al. [124] have described a novel application of the PIXE method. They investigated the elemental composition of earthworm fecal material and the linings of earthworm channels. The worms were taken from an experimental agricultural plot which had been given applications of sewage sludge over an eight year period. Thin sections (50  $\mu\text{m}$  from  $8 \times 9 \times 5 \text{ cm}^3$  soil samples which had been impregnated with 3-hydroxyl butyl methyl methacrylate (3-HBMA). A 5  $\mu\text{m}$  proton beam was used to measure concentrations over a  $400 \mu\text{m} \times 400 \mu\text{m}$  region around the earthworm burrow and the adjacent soil found at a depth of 40–45 cm below the surface. Figure 5.2 10 [124] shows the PIXE spectra obtained for the two regions. The region around the burrow are shown to be highly enriched in many elements including Cu, Zn, and Pb. Fecal composition for soil close to the surface was identified by regions of high P content. In those regions the elemental composition was increased by an order of magnitude when compared to the concentrations found at the deeper level. This experiment demonstrates an important application for PIXE which require its many unique features. Extension of the scope of the experiment to measurement of the uptake of these elements in the worms would make it possible to understand the biological pathways for these elements in the worm in addition to determining the importance of their transport in the soil. There should be many future applications in soil science and in related studies of toxicity effects on marine organisms living in and around contaminated sediments.

## 5.3. ACCELERATOR MASS SPECTROMETRY

### Introduction

AMS incorporates an ion accelerator and its beam transport system as elements of an ultra-sensitive mass and charge spectrometer. Multiple selection stages for energy, momentum, velocity and atomic charge plus final identification of nuclear mass and charge with an ion detector makes possible measurements of isotopic ratios some four or five orders of magnitude smaller than is possible with conventional mass spectrometry (MS). The high selectivity of AMS enables a dramatic reduction of the backgrounds that plague MS: molecular and isobaric interferences and tails of abundant neighbouring masses. For instance, AMS allows an isotopic sensitivity of less than one part in  $10^{15}$  for  $^{14}\text{C}$ ,  $^{10}\text{Be}$  and other radionuclides occurring in nature at ultra-trace levels (see Table 5.3.1). The sensitivity of AMS is unaffected by the half-life of the isotope being

Table 5.3.1  
Key information of radionuclides commonly measured by AMS

Radioisotope	$^{10}\text{Be}$	$^{14}\text{C}$	$^{26}\text{Al}$	$^{36}\text{Cl}$	$^{129}\text{I}$
Stable isotopes	$^9\text{Be}$	$^{12}\text{C}$ , $^{13}\text{C}$	$^{27}\text{Al}$	$^{35}\text{Cl}$ , $^{37}\text{Cl}$	$^{127}\text{I}$
Interfering isobars	$^{10}\text{B}$	$(^{14}\text{N})^*$	$(^{26}\text{Mg})^*$	$^{36}\text{S}$	$(^{129}\text{Xe})^*$
Chemical form <sup>a</sup>	BeO	C	$\text{Al}_2\text{O}_3$	AgCl	AgI
Sample size [mg] <sup>b</sup>	2	0.5	2	5	5
Background <sup>c</sup>	$2-3 \times 10^{-15}$	$1 \times 10^{-15}$	$2-3 \times 10^{-15}$	$1 \times 10^{-15}$	$20 \times 10^{-15}$
Detection limit <sup>d</sup>	$10^6$	$10^6$	$10^7$	$10^6$	$10^7$
Precision [%] <sup>e</sup>	3	1	3	3	3

<sup>a</sup>Graphite is commonly used for carbon.

<sup>b</sup>Carrier material is added in some cases to bring the sample weight to that shown in the table.

<sup>c</sup>The lowest isotopic ratio that can be measured. It is determined by instrumental background (interfering ions which reach the detector and have not been separated from the radioisotope) and contamination (radioisotope ions which are not intrinsic to the original sample material).

<sup>d</sup>The number of radioisotope atoms in the original sample needed to obtain the precision shown in the table (for an abundance of  $10^{-12}$ ).

<sup>e</sup>Typical statistical error in AMS measurement of these isotopes.

\* These isobars do not form negative ions.

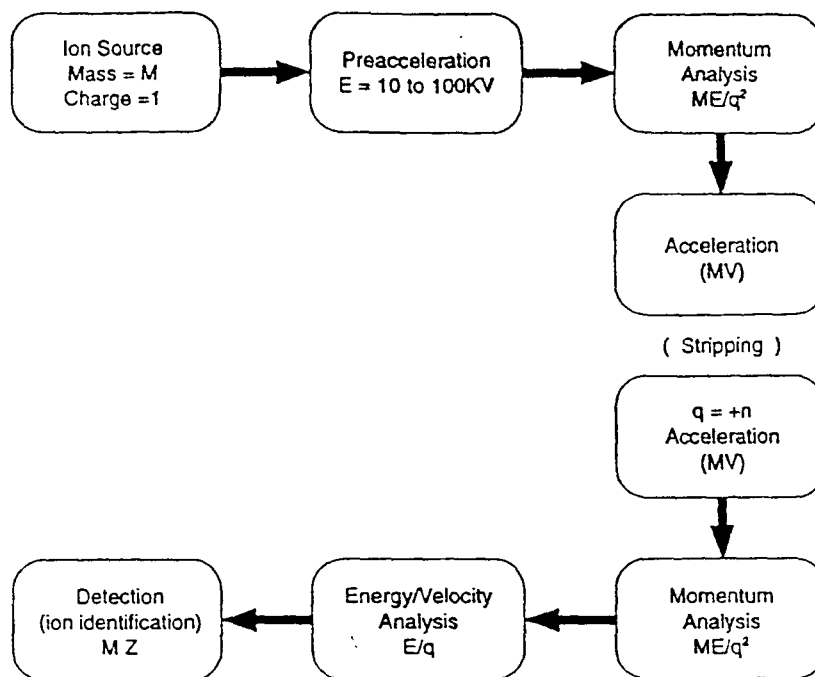


Figure 5.3.1. Schematic layout spectrometer.

measured, since the atoms not the radiations that result from their decay are counted directly. Hence, the efficiency in the detection of the aforementioned radionuclides improves by several orders of magnitude, depending on the half-life of the radionuclide being measured. The size of the sample required for the analysis is reduced accordingly. Also some stable isotopes, often present in the environment at very low concentrations, such as the rare earth elements (REE) and the platinum group elements (PGE), can be detected by AMS with better sensitivities than low-energy MS.

In the last 15 years, AMS systems have been developed at more than 40 laboratories for the detection of low-abundance radionuclides in environmental, archaeological, biomedical and industrial samples [125–128].

Electrostatic tandem accelerators are the optimum choice for a variety of AMS applications. Small tandems (1.7–3 MV) have been specifically designed for  $^{14}\text{C}$  analysis [129]. These relatively low-energy tandems can also be used to detect other long-lived radionuclides, such as  $^{10}\text{Be}$ ,  $^{26}\text{Al}$  and  $^{129}\text{I}$  or stable isotopes. Larger tandem accelerators, originally used for nuclear physics research, can be upgraded and used to analyse a variety of rare radionuclides [130].

Other accelerators, such as cyclotrons, have been also used in AMS. Cyclotrons allow the achievement of high ion energies by repeated application of relatively low electrostatic fields. However, the principle of cyclotron operation applies only to a specific ion mass so that it can be used to reject unwanted masses with high resolution. Cyclotrons were used for early AMS measurements of some long-lived cosmogenic radionuclides such as  $^{10}\text{Be}$  [131] and  $^{26}\text{Al}$  [132]. A mini cyclotron has been used to detect  $^{14}\text{C}$  at natural abundances, but the practical use of this system will require further developments to allow precise measurements of isotopic ratios [133].

### 5.3.1. AMS with tandem accelerators

In AMS, the element of interest is chemically separated from the original sample and loaded as a target in the sputter ion source of the tandem accelerator.

A schematic diagram of a tandem-based AMS system is shown in Figure 5.3.1. Negative ions are produced in the ion source, and after optional energy analysis, are pre-accelerated to an energy  $E=10\text{-}100\text{keV}$ . The ion mass is then analysed by a magnetic field. After their injection into the accelerator, negative ions are attracted by the positive voltage at the terminal and thereby accelerated to high energies (a few megaelectronvolts), at which point they pass through a gas or a foil stripper located at the terminal and stripped of some of their electrons. Multi-charged positive ions are then further accelerated by the same positive voltage on the terminal. Following the acceleration, combinations of magnetic and electric fields select momentum, energy and velocity of the ions. High-resolution Wien filters, electrostatic analysers, and double focusing magnets provide the selectivity necessary to separate the radionuclide of interest. Finally, the identification of the rare isotope, accelerated to energies of  $10\text{-}100\text{ MeV}$ , is performed in the ion detector. Depending on the isotopes to be counted, a variety of detectors are available for this final stage of the AMS spectrometer such as ionisation chambers and time-of-flight detectors. Energy, stopping power, range and velocity can be measured to identify the isotopes of interest. Determination of isotopic ratios requires also the measurement (with Faraday cups) of currents from abundant isotopes.

The main advantages of tandems for AMS are firstly, the use of sputter sources producing negative ions and secondly, terminal stripping. The first feature is important as most elements form negative ions and many radionuclides can be analysed. In addition, there are some favorable cases where the interfering isobar does **not** produce negative ions, e.g.  $^{14}\text{N}$  in the analysis of  $^{14}\text{C}$  and  $^{26}\text{Mg}$  in the detection of  $^{26}\text{Al}$ . The stripping of three or more electrons at the terminal of the tandem is a powerful stage to reject molecular interferences which are the main limitation for conventional MS.

High precision AMS analysis is carried out by either using simultaneous injection or rapid sequential injection of the isotopes of interest, in order to overcome variability in source output and accelerator transmission. Simultaneous injection restricts the range of masses analysed and has been recently adopted in commercial accelerators dedicated to radiocarbon analysis. Sequential injection allows the development of a more universal system, suitable for the high precision analysis of a wide range of nuclides.

### 5.3.2. AMS microprobes

Secondary Ion Mass Spectrometry (SIMS) is used for isotopic analysis with high sensitivity and micron-size space resolution. It makes use of a sputter ion source and a mass spectrometer for analysis and detection of the keV secondary particles (positive, negative or neutral) produced. The use in a SIMS system of an AMS spectrometer improves the detection limit for many elements by several orders of magnitude. This technique is sometimes referred to as super-SIMS.

The first studies with super-SIMS systems showed that limitations arise from contamination by impurities in the Cs sputtering beam and from materials used in the construction of the ion source [134]. Special designs have therefore been developed using magnetic analysis of the sputtering beam and construction of the source from high purity silicon [134]. The super-SIMS system developed at the University of North Texas and Texas Instruments, allows bulk sensitivities of  $10^{13}$  atoms/cm<sup>3</sup> for several elements in the periodic table and may be used for both bulk and depth profiling measurements.

Super-SIMS does not require high acceleration energy and 2 to 3 MV tandems can be used for the determination of trace elements in geological samples [135].

### 5.3.3. Long-lived radionuclides

Radionuclides are used as tracers and chronometers in many disciplines: geology, archaeology, astrophysics, biomedicine and materials science. Low-level decay counting techniques have been developed in the last half century to detect the concentration of cosmogenic, radiogenic and anthropogenic radionuclides in a variety of specimens. The radioactivity measurement for long-lived cosmogenic radionuclides, such as  $^{10}\text{Be}$ ,  $^{14}\text{C}$ ,  $^{26}\text{Al}$ , and  $^{36}\text{Cl}$ , is made difficult by low counting rates and in some cases the need for complicated radiochemistry procedures and efficient

detectors of soft beta particles and low energy X-rays. AMS can measure cosmogenic radionuclides in geological samples up to  $10^6$  times smaller than those required for conventional techniques, allowing novel applications in geology and environmental science.

### *Atmospheric production*

$^{10}\text{Be}$  is produced by cosmic ray spallation on atmospheric  $^{14}\text{N}$  and  $^{16}\text{O}$  ( $5 \times 10^2$  atom  $\text{m}^{-2} \text{s}^{-1}$ ) and is quickly scavenged by aerosol particles. Atmospheric residence time is about one or two years.  $^{10}\text{Be}$  precipitation provides the signature in soils and sediments due to the strong particle-binding affinity of Be. Atmospheric  $^{10}\text{Be}$  is used as a tracer and a chronometer to study: sedimentation rates in lacustrine and marine sediments; continental erosion rates by soil tracing and inventories; and formation time scales of marine nodules.

$^{36}\text{Cl}$  is produced in the atmosphere mainly by cosmic ray spallation of  $^{40}\text{Ar}$ . As a consequence of the hydrophilic nature of Cl, meteoric  $^{36}\text{Cl}$  readily enters the hydrosphere and can be used to date old groundwaters. The  $^{36}\text{Cl}$  production rate in the atmosphere varies with latitude from 3 to 30 atom  $\text{m}^{-2} \text{s}^{-1}$ . Meteoric  $^{36}\text{Cl}$  is diluted by Cl in marine aerosols; the resulting  $^{36}\text{Cl}/\text{Cl}$  ratio may range from  $10^{-14}$  near the coast to  $10^{-12}$  in continental interiors.

$^{14}\text{C}$  is produced in the upper atmosphere by secondary thermal neutrons reacting with  $^{14}\text{N}$  and enters the carbon cycle. The production rate is  $2.5 \times 10^4$   $\text{m}^{-2} \text{s}^{-1}$  with a global inventory of  $3 \times 10^{30}$  atoms (90% oceans, 8% biosphere and soils, 2% atmosphere). Equilibrium is reached between cosmogenic production and radioactive decay of  $^{14}\text{C}$  with a natural (pre-nuclear-era) isotopic concentration for atmospheric carbon of  $1.2 \times 10^{-12}$ . All living organisms exchange carbon with the atmosphere and are characterised by this  $^{14}\text{C}/^{12}\text{C}$  ratio. When a living organism dies, the carbon exchange stops. Hence, by measuring the residual  $^{14}\text{C}$  concentration in organic samples, it is possible to calculate the time elapsed since the material was in equilibrium with the atmosphere (radiocarbon dating). Ages between 300 yr BP (before present) and 50,000 yr BP can be detected by this technique.

$^{129}\text{I}$  is produced in the atmosphere by cosmic rays interacting with xenon. Iodine-containing formations such as halite deposits, brines, marine sediments and oil shale could be "dated" with  $^{129}\text{I}$ , provided radiogenic contribution is corrected for.

$^{26}\text{Al}$  is produced in the atmosphere by spallation of  $^{40}\text{Ar}$ , at a rate 1/300 that of  $^{10}\text{Be}$ . The high natural abundance of stable Al ( $^{27}\text{Al}$ ) in terrestrial materials makes the ratio  $^{26}\text{Al}/^{27}\text{Al}$  very small, close to the limit of AMS detection.

Long-lived radionuclides produced at the top of the atmosphere are delivered to the Earth's surface and accumulated in chronological sequence in more or less undisturbed reservoirs, such as polar ice, marine sediments, tree rings, corals, soils etc. Some of these collectors can be dated by independent techniques. Ice chronology is obtained from seasonal cycles ( $\delta^{18}\text{O}$  method); sedimentation rates are used to provide age of sediments; dendrochronology can be used to date trees and coral samples. Measurement of cosmogenic radionuclides in these archives allows the observation of variations in production rates induced by changes in solar activity, geomagnetic excursions and other cosmochronologic effects. The radionuclide concentration in these reservoirs is also modulated by climatic changes in the past and other factors influencing their transport and deposition.

Polar ice is an archive where deposition of natural radionuclides extends back in the past for  $10^4$ – $10^5$  a and radionuclides such as  $^{10}\text{Be}$ ,  $^{14}\text{C}$  and  $^{36}\text{Cl}$  can be measured with high temporal resolution (1–10 a). The present accumulation rate in Antarctica is about 14 cm of water-equivalent per year. Cores of about 2000 m are drilled and 1 kg of ice is sufficient for AMS measurements. The deposition rate in ice is strongly influenced by atmospheric processes, but climatic and cosmochronological effects can be separated, in principle, by measuring different cosmogenic radionuclides.

One of these cosmogenic radionuclides,  $^{10}\text{Be}$ , incident on the ocean accumulates finally in deep sea sediments. The sedimentation rates in open oceans are of the order of 1 mm per  $10^3$  a. Cores accumulated in  $10^7$ – $10^8$  years have been studied, with a temporal resolution of  $10^5$  a. The high  $^{10}\text{Be}$  concentration in deep sea sediments has been used to trace their recycling through the volcanic systems of convergent plate margins.

### *In situ* production

Cosmogenic radionuclides are also produced *in situ*, on the Earth's surface and the determination of their production provides a powerful method for studying processes affecting production rates. Examples of applications include: dating volcanic flows; dating meteorite impacts; determination of erosion rates and exposure ages of surfaces; and dating glacial stages via moraines, pavements and boulders. Neutrons dominate nuclide production in the top few meters of the Earth's surface and muons become important at larger depths. Contamination from atmospheric cosmogenic radionuclides hampers in many cases the identification of *in situ* produced cosmogenic radionuclides. In specific cases, this distinction becomes possible. For example, *in situ* produced  $^{10}\text{Be}$  and  $^{26}\text{Al}$  have been identified in quartz, in impact ejecta and in olivines from lava flows. Quartz is a mineral that occurs in many materials of geological importance and is subjected to alteration with a very slow rate.

The build-up process can be expressed by the following expression (if  $P(l,a) \ll \lambda$ ):

$$C_e = \frac{P(l;a)}{\lambda + \rho\eta/\Lambda} (1 - e^{-(\lambda + \rho\eta/\Lambda)t}) e^{-\rho d/\Lambda} \quad (5.3.1)$$

where  $C$  is the  $^{10}\text{Be}$  concentration (with no erosion),  $P$  is the production rate, function of latitude ( $l$ ) and altitude ( $a$ ),  $\lambda$  is the decay constant,  $\Lambda$  is the mass attenuation length (about  $150 \text{ g/cm}^2$  for nucleonic production),  $d$  is the depth below surface and  $\rho$  is the density of the material (about  $3.5 \text{ g/cm}^3$ ).

In presence of constant erosion, the above formula becomes

$$C_e = \frac{P(l;a)}{\lambda + \rho\eta/\Lambda} (1 - e^{-\lambda t}) e^{-\rho d/\Lambda} \quad (5.3.2)$$

where  $\eta$  is the rate of erosion.

At secular equilibrium, the isotope concentration at the surface ( $d=0$ ) becomes

$$C_{0e} = \frac{P(l;a)}{\lambda + \rho\eta/\Lambda} \quad (5.3.3)$$

from which the following expression for the erosion rate is obtained:

$$\eta = \frac{\Lambda\lambda}{\rho} \left( \frac{C_0}{C_{0e}} - 1 \right) \quad (5.3.4)$$

where  $C_0$  is the concentration of the radionuclide with no erosion and  $C_{0e}$  is the measured value.

$^{10}\text{Be}$  is produced in quartz, via fast neutron and muon interactions on  $^{16}\text{O}$ , within a few meters of the surface, at a rate of  $6 \text{ atom g}^{-1} \text{ a}^{-1}$ , at geomagnetic latitudes of  $50$ – $90$  degree at sea level. The crystal structure of quartz prevents contamination from meteoric  $^{10}\text{Be}$  and acts as a closed system for  $^{10}\text{Be}$  build-up to secular equilibrium for exposures of a few million years. AMS detection of this *in situ*  $^{10}\text{Be}$  signal is possible in tens of gram of rock exposed for as little as  $10^3$  a.

*In situ* production of  $^{26}\text{Al}$  (in the same condition) is  $36 \text{ atom g}^{-1} \text{ a}^{-1}$ . The low levels of Al in quartz (tens of ppm) result in  $^{26}\text{Al}/\text{Al}$  ratios as high as  $10^{-11}$  that are easily measurable by AMS. A model describing the irradiation history of rock surfaces based on  $^{26}\text{Al}/^{10}\text{Be}$  *in situ* ratios has been developed and calibrated. Exposure ages ranging from  $5 \times 10^3$  to  $5 \times 10^6$  a and erosion rates ranging from  $10^{-2}$  to  $10^{-5} \text{ cm a}^{-1}$  can be determined.

$^{36}\text{Cl}$  is produced *in situ* by spallation reactions ( $^{39}\text{K}(n,x)^{36}\text{Cl}$ ,  $^{40}\text{Ca}(n,x)^{36}\text{Cl}$ ) and thermal neutron capture ( $^{35}\text{Cl}(n,\gamma)^{36}\text{Cl}$ ,  $^{39}\text{K}(n,\alpha)^{36}\text{Cl}$ ), which predominate in the first few meters of the Earth's surface; and capture of muons, which penetrate  $\sim 100 \text{ m}$  ( $^{39}\text{K}(\mu,x)^{36}\text{Cl}$ ,  $^{40}\text{Ca}(\mu,x)^{36}\text{Cl}$ ). The  $^{36}\text{Cl}$  thus produced builds up to an equilibrium concentration, typically in the range  $0.1$ – $20 \times 10^6 \text{ atom g}^{-1}$ , depending on the concentration of Cl, K and Ca in the rock.

Also  $^{14}\text{C}$  is produced *in situ* by neutrons and muons incident on the terrestrial surface. The  $^{14}\text{C}$  production rate in quartz (at sea level) is  $20 \text{ atom g}^{-1} \text{ a}^{-1}$ .

#### *Radiogenic production*

$^{14}\text{C}$  can be produced underground by the decay of uranium and thorium series. An estimate of this  $^{14}\text{C}$  can be useful in the study of hydrological environments where uranium and thorium are high.

Production of  $^{36}\text{Cl}$  in the sub-surface occurs due to neutron flux generated by  $\alpha$ -particles from U and Th decay resulting from the n-induced reactions  $^{35}\text{Cl}(n,\gamma)^{36}\text{Cl}$  and  $^{39}\text{K}(n,\alpha)^{36}\text{Cl}$ . This results in concentrations ranging from  $2 \times 10^2$  to  $1 \times 10^5 \text{ atom g}^{-1}$  depending on the concentration of U, Th and suitable materials in the rock. Where, groundwaters pass through a high neutron flux environment, such as granitic rocks or close to U ore, neutron capture reactions on dissolved chloride results in an ingrowth of  $^{36}\text{Cl}$ . The level of ingrowth can be used to calculate the residence time of the water in the high-flux region.

$^{129}\text{I}$  is produced in U-rich rocks by spontaneous fission of  $^{238}\text{U}$  (99.27%) and by neutron induced fission of  $^{235}\text{U}$  (0.72%). This  $^{129}\text{I}$  may be leached out of rocks into surrounding waters and other fluids. The accumulation of  $^{129}\text{I}$  in groundwaters, brines and oil shales has been studied to evaluate the contribution from radiogenic and atmospheric  $^{129}\text{I}$ . These two sources of  $^{129}\text{I}$  contribute approximately equal quantities to the hydrosphere. Close to uranium ore bodies  $^{129}\text{I}$  levels can be very high, making it a useful tracer for fission product migration in these environments.

#### *Anthropogenic production*

Long-lived radionuclides are also produced by nuclear technology and periodically released into the environment. They can be used as environmental tracers in various applications.

For example, the natural abundance of  $^{129}\text{I}$  is estimated to be  $10^{-12}$  (Fehn, 1986). It is well known that the concentration of  $^{129}\text{I}$  in the environment is today orders of magnitude higher than its natural level. In fact, artificial  $^{129}\text{I}$  is produced by thermal neutron induced fission of  $^{235}\text{U}$  and  $^{239}\text{Pu}$  from nuclear fuel reprocessing facilities and reactor facilities and weapon testing.  $^{129}\text{I}$  has a low specific activity ( $6.51 \times 10^6 \text{ Bq/g}$ ) decaying with the emission of a beta particle ( $E_{\beta\text{max}} = 150 \text{ keV}$ ) and is not considered a biological hazard.

This signal of anthropogenic  $^{129}\text{I}$  is archived in a variety of both global and local environmental settings. Few measurements of  $^{129}\text{I}$  in the environment have been performed due to difficulty of its detection. Decay counting is not practical for the low efficiency due to the long half-life of  $^{129}\text{I}$ . NAA techniques have been utilised in the test for samples collected near nuclear power plants [137]. This method is very complex and large samples are required. Using AMS the expected low-level concentrations of  $^{129}\text{I}$  can readily be measured, leading to an understanding of its global inventory and transport, and subsequently its use as a monitor of nuclear activity.

AMS has been recently used to study the  $^{129}\text{I}$  emission from the Sellafield Nuclear Fuel Reprocessing Plant [138]. In this study,  $^{129}\text{I}$  has been analysed in moss down-wind from the Sellafield Nuclear Fuel Reprocessing Plant. Moss derives its nutrients from the atmosphere and can be used as an indicator of past input of  $^{129}\text{I}$  from the reprocessing plant. Isotopic ratios  $^{129}\text{I}/^{127}\text{I}$  ranges from  $10^{-4}$ – $10^{-7}$ , several orders of magnitude higher than background levels. Seaweed from Atlantic and Pacific shores have  $^{129}\text{I}/^{127}\text{I} = 10^{-11}$  in the post-bomb period and  $10^{-10}$  in the pre-bomb period [139]. One milligram dry moss is sufficient for this kind of analysis.

Ice cores corresponding to the past 50 years preserve an annual record of variations in  $^{129}\text{I}$  levels. The  $^{129}\text{I}$  concentrations in these ice cores can be applied to available global transport models to evaluate the pre-bomb and post-bomb  $^{129}\text{I}$  inventories, and atmospheric and exchange rates.  $^{129}\text{I}$  sampled from natural archives in proximity of either nuclear weapons test sites and power plants can be compared to expected global levels and thus employed to detect and monitor irregular or unacceptable behaviour.

The atmospheric bomb test in the 1950's produced a  $^{36}\text{Cl}$  spike at 1000 times natural levels (a useful tracer for recent water flows). High levels are also measured near nuclear facilities [140].

$^{14}\text{C}$  levels in the atmosphere show a major peak in 1963 (with about 10% increase in  $^{14}\text{C}$  concentration). This bomb pulse is useful to study environmental problems such as the air

enclosure process in ice. The effect of power reactors in the incorporation of  $^{14}\text{C}$  in environmental samples has been also studied.

#### 5.3.4. Stable nuclides

Novel applications in geoscience and materials science require the detection of stable nuclides at the ultra-trace level, below the detection limit possible with conventional techniques such as MS, SIMS and ICP-MS. AMS has demonstrated detection limits in the sub-ppm to ppb range for PGE, REE and Au.

An AMS facility, AUSTRALIS, dedicated to the *in situ* microanalysis of geological samples, is being developed in Sydney [141]. This system is based on a 3 MV Tandem accelerator and a modified General Ionex model 834. New features of this system are the analysed and focused Cs microbeam and fast isotope switching at the high energy end using deflecting electrodes. AUSTRALIS will be applied in studies of trace element geochemistry for which the PIXE microprobe is not suitable. Trace elements lighter than the ubiquitous Fe element are difficult to detect with PIXE and with AMS could be detected at sub-ppm levels. PIXE has poor sensitivity also for heavy elements. The AUSTRALIS system will be used to measure the fractionation of PGE and REE in petrogenic studies. Other applications are related to detect precious metal distribution in ore minerals.

#### 5.3.5. Actinides

Many groups are presently developing AMS analysis of actinides, in particular  $^{236}\text{U}$  and  $^{233}\text{U}$  in uranium and  $^{229}\text{Th}$  and  $^{230}\text{Th}$  in thorium.  $^{236}\text{U}$  ( $T_{1/2}=23.4$  Ma) is particularly interesting for safeguards monitoring and as a neutron flux integrator in geological applications.  $^{236}\text{U}$  is produced by neutron capture on  $^{235}\text{U}$  and from the  $\alpha$ -decay of  $^{240}\text{Pu}$  (produced in nuclear reactors).  $^{236}\text{U}$  has never been systematically analysed in natural samples for the limited sensitivity of conventional MS in the measurement of its isotopic concentration. The Tandem at IsoTrace Laboratory, operating at 2.5 MV, has been recently used to measure a  $^{236}\text{U}/^{238}\text{U}$  ratio of  $4 \times 10^{-10}$  in samples from a uranium ore [142], [143]. AMS should be capable of detecting  $^{236}\text{U}/^{238}\text{U}$  at concentrations of  $10^{-13}$ , which is the ratio expected in the environment before the nuclear era.

The main limitation of low-voltage AMS systems is that a narrow range of charge states are available to optimize the detection selectivity. On the other hand, the use of high terminal voltages (5–10 MV) for AMS of heavy isotopes is hindered by the necessity of using magnets of prohibitive cost for the high energy analysis. Alternative high-energy AMS spectrometers are being constructed for actinide work, with a high resolution injector and an all-electrostatic post acceleration system [144]. This kind of spectrometer can be used for the detection of actinides with half-lives larger than 1000 years. There are many cases where AMS identification of the specific nuclide is easy because of the lack of isobaric interferences. The development of AMS techniques for the analysis of heavy ( $M \sim 200$  amu) isotopes at terminal voltage of 5–10 MV has not been adequately followed up.

#### 5.3.6. Acknowledgement

The support of the US-Hungarian Joint Fund (111/91) is acknowledged. The authors are indebted to Miss Lora Barbier for the careful collection of material and preparation of the text (K.J.). Work supported in part by US Department of Energy Contract No. DE-AC02 98CH10886 (K.J.).

#### 5. 4. REFERENCES

1. B. Yun, P. J. Viccaro, B. Lai, J. Chrzas, *Rev. Sci. Instrum.* 63, 582–585 (1992).
2. A. Robinson, *Synchrotron Radiation News* 6, 35 (1993).
3. R. P. Walker, *Rev. Sci. Instrum.* 63, 1615–1620 (1992).
4. V. Korchuganov, *Synchrotron Radiation News* 6, 18–19 (1993).
5. M. Yoon, *Synchrotron Radiation News* 5, 110–112 (1992).
6. A. Craievich, *Synchrotron Radiation News* 6, 4–5 (1993).
7. C. N. Archie, J. I. Granlund, R. W. Hill, K. W. Kukkonen, J. A. Leavey, L. G. Lesoine, J. M. Oberschmidt, A. E. Palumbo, C. J. Wasik, *Vac. Sci. Technol.* 10, 3224–3228 (1992).

8. M. N. Wilson, A. I. C. Smith, M. C. Townsend, J. C. Schouten, R. J. Anderson, A. R. Jordan, V. P. Suller, M. W. Poole, *IBM Y. Res. Develop* 37, 351-369 (1993).
9. M. Ando, *Synchrotron Radiation News* 6, 19-30 (1993).
10. F. REider, A. Gurenwitsch, Langmuir, H. C. Pollock, *Phys. Rev.* 71, 829 (1947).
11. H. Winick, Properties of Synchrotron Radiation, in *Synchrotron Radiation Research* Eds.: H. Winick and S. Doniach, *Plenum Press*, New York, (1980).
12. Kwang-Je Kim, *X-ray Data Booklet* (D. Vaughan Ed.), Lawrence Berkeley Laboratory
13. J. V. Smith, L. Rivers; *Synchrotron X-ray Microanalysis*, in *Microprobe Techniques in the Earth Sciences* (ed. P. J. Potts), *Chapman and Hall*, London (1994).
14. K. W. Jones, *Synchrotron Radiation-Induced X-ray emission*, in *Handbook of X-ray Spectrometry*, Van Grieken, R. E. and A. A. Markowicz, ed. *Marcel Dekker*, New York, p. 411-452, (1993).
15. G. Schmall, D. Rudolph, ed. *X-ray Microscopy*, *Springer*, Berlin (1984).
16. A. Knöchel, W. Petersen, G. Tolkien, *Nucl. Instr. Methods* 208, 659 (1983).
17. K. W. Jones, W. M. Kwiatek, B. M. Gordon, A. L. Hanson, J. G. Pounds, M. L. Rivers, S. R. Sutton, A. C. Thompson, J. H. Underwood, R. D. Giaque, Y. Wu, *Adv. X-ray Anal.* 31, 59, (1988).
18. K. W. Jones, B. M. Gordon, G. Schidlovsky, P. Spanne, Xue Dejun, R. S. Bockman, A. J. Saubermann, in *Microbeam Analysis 1990* D. B. Williams, P. Indgram, J. R. Michels, Eds.), *San Francisco Press*, San Francisco, pp. 401-404, (1990).
19. W. M. Kwiatek, A. L. Hanson, K. W. Jones, *Nucl. Instr. Methods Phys. Res.* B50, 347 (1990)
20. P. Chevallier, C. Jehanno, M. Maurette, S. R. Sutton, J. Wang, *J. Geophys. Res.*, 192(B4), E649 (1987).
21. F. Van Langevelde, G. H. Tros, D. K. Bowen, R. D. Vis, *Nucl. Instr. Methods Phys. Res.*, B49, 544 (1990).
22. A. C. Thompson, Y. Wu, J. H. Underwood, T. W. Barbee, *Nucl. Instr. Methods Phys. Res.* A255, 603 (1987).
23. Y. Wu, A. C. Thompson, J. H. Underwood, R. D. Giaque, K. Chapman, M. L. Rivers, K. W. Jones, *Nucl. Instr. Methods Phys. Res.* A291, 146 (1990)
24. K. Saitoh, K. Inagawa, K. Kohra, C. Hayashi, *Rev. Sci. Instrum.* 60, 1519 (1989).
25. D. Carpenter, R. L. Lawson, M. A. Taylor, D. E. Poirier, K. Z. Morgan, G. W. Haney, *Microbeam Analysis*, 391 (1981)
26. A. J. Bos, R. D. Vis, H. Verheul, R. Prins, K. D. Bowen, J. Makjanic, V. Valkovic, *Nucl. Instrum. Methods*, B3, 232 (1984).
27. F. Van Langevelde, K. D. Bowen, G. H. Tros, R. D. Vis, A. Huizing, D. de Boer, *Nucl. Instrum. Methods*, A292, 719 (1990).
28. S. Török, Z. Szökéfalvi-Nagy, S. Sándor, V. Baryshev, K. Zolotarev, G. N. Kulipanov, *Nucl. Instrum. Methods*, A282, 499 (1989).
29. K. Janssens, F. Van Langevelde, F. C. Adams, R. D. Vis, S. R. Sutton, M. L. Rivers, K. W. Jones, D. K. Bowen, *Adv. X-ray Anal.* 38, 215 (1992).
30. K. W. Jones, B. M. Gordon, *Anal. Chem.* 61, 341A (1989).
31. S. Hayakawa, A. Iida, S. Aoki, Y. Gohshi, *Rev. Sci. Instr.* 60, 2452 (1989).
32. J. V. Smith and M. L. Rivers. *Synchrotron X-ray microanalysis*. In *Microprobe Techniques in the Earth Sciences*, P. J. Potts, J. F. W. Bowles, S. J. B. Reed, M. R. Cave, Eds. *Chapman & Hall*, London, pp. 163-233, (1995).
33. J. V. Smith, *Analyst* 120, 1231-1245 (1995).
34. A. Iida, *trends in analytical chemistry*, 10, 215 (1991).
35. C. Tuniz, F. Zanini, K. W. Jones, *Nucl. Instr. Methods*, 1B56'57, 877 (1991).
36. S. R. Sutton, M. L. Rivers, S. Bajt, K. Jones, J. V. Smith, *Nucl. Instr. Methods*, A347, 412 (1994).
37. M. Pennisi, M. F. Cloarec, G. Lambert, J. C. Le Rouley, *Earth Planet. Sci. Lett.* 88, 284 (1988).
38. G. J. Flynn, S. R. Sutton, S. Bajt, *Lunar Planet. Sci.* XXIV, 495 (1993).
39. S. R. Sutton, G. J. Flynn, *Proc. Lunar Planet. Sci. Conf.* 20, 357 (1990).
40. J. R. Chen, E. C. Chao, J. A. Minkin, J. M. Back, W. C. Bagby, M. L. Rivers, S. R. Sutton, B. M. Gordon, A. L. Hanson, K. W. Jones, *Nucl. Instrum. Methods*, B22, 394 (1987).
41. R. N. White, D. A. Spears, J. V. Smith, *Synchrotron X-ray fluorescence trace element analysis of sulfides in United Kingdom coal*, (abstract) GSA Meeting, (1987).
42. J. Meijer, A. Stephan, J. Adamczewski, H. H. Bukow, C. Rolfs, T. Pickart, F. Bruhn, J. Veizer, *Nucl. Instrum. Methods*, B89, 229-232 (1994).
43. H. Kucha, W. Przybyłowicz, M. Lankosz, F. van Langevelde, K. Traxel, *Mineralogical Magazine*, 57, 103-112 (1993).
44. W. L. Griffin, J. J. Gurney, C. G. Ryan, *Contrib. Mineral. Petrol.*, 110, 1-15 (1992).
45. C. A. Heinnch, C. G. Ryan, T. P. Memagh, P. J. Eadington, *Econ. Geol.*, 87, 1566-1583 (1992).
46. E. E. Horn and K. Traxel, *Chem. Geol.*, 61, 29-35 (1987).
47. J. D. Frantz, H. K. Mao, Yi-gang Zhang, Y. Wu, A. C. Thompson, J. H. Underwood, R. D. Giaque, K. W. Jones, M. L. Rivers, *Chem. Geol.*, 69, 235-244 (1988).
48. J. L. Campbell. Applications in earth sciences. In *Particle-Induced X-Ray Emission Spectrometry*, S. A. E. Johansson, J. L. Campbell, K. G. Malmqvist, Eds., *Chemical Analysis Series*, Vol. 133, *John Wiley & Sons*, pp. 313-365, (1995).
49. S. H. Sie, W. L. Griffin, C. G. Ryan, G. F. Suter, D. R. Cousens, *Nucl. Instrum. Methods*, B54, 284-291 (1991).
50. J. R. Tesmer and M. Nastasi, Editors; J. C. Barbour, C. J. Maggiore, J. W. Mayer, Contributing Eds., *Handbook of Modern Ion Beam Materials Analysis*, *Materials Research Society*, Pittsburgh, PA 15237 (1995).
51. Z. B. Alfassi, Ed., *Chemical Analysis by Nuclear Methods*, *John Wiley & Sons*, New York, (1994).
52. Z. B. Alfassi and M. Peisach, *Elemental Analysis by Particle Accelerators*, *CRC Press*, Boca Raton, FL (1992).

97. L. J. Cabri, L. J. Hulbert, J. H. G. Laflamme, R. Lastra, S. H. Sie, C. G. Ryan, J. L. Campbell, *Explor. Mining Geol.*, 2(2), 105-119 (1993).
98. L. J. Cabri and Greg McMahon, *The Canadian Mineralogist* 33, 349-359 (1995).
99. J. L. Campbell, J. A. Maxwell, W. J. Teesdale, J.-X. Wang, L. J. Cabri, *Nucl. Instr. Methods* B44, 347-356 (1990).
100. G. K. Czamanske, V. E. Kuniilov, M. L. Zientek, L. J. Cabri, A. P. Likhachev, L. C. Calk, Robert L. Oscarson, *The Canadian Mineralogist*, 30, 249-287 (1992).
101. A. J. Criddle, H. Tamana, J. Spratt, K. J. Reeson, D. Vaughan, G. Grime, *Nucl. Instr. Methods* B77, 444-449 (1993).
102. K. Hatton, L. J. Cabri, S. R. Hart, *Contrib. Mineral. Petrol* 109, 10-18 (1991).
103. A. C. L. Larocque, Jennifer A. Jackman, Louis J. Cabri, C. Jay Hodgson, *The Canadian Mineralogist* 33, 361-372 (1995).
104. A. C. L. Larocque, C. Jay Hodgson, L. Cabri, Jennifer A. Jackman, *The Canadian Mineralogist* 33, 373-388 (1995).
105. P. Neumayr, L. J. Cabri, D. J. Groves, E. J. Mikucki, J. A. Jackman, *The Canadian Mineralogist* 31, 711-725 (1993).
106. W. Przybyšowicz, A. Piestrzynski, K. Traxel, S. Bajt, *Nucl. Instr. Methods* B49, 509-513 (1990).
107. W. Przybyšowicz, H. Kucha, A. Prestrzynski, K. Traxel, S. Bajt, *Nucl. Instr. Methods* B50, 231-237 (1990).
108. J. C. Rucklidge, Graham C. Wilson, Linas R. Kilius, Louis J. Cabri., *The Canadian Mineralogist* 30, 1023-1032 (1992).
109. H. Tamana, A. Criddle, G. Grime, D. Vaughan, J. Spratt, *Nucl. Instr. Methods* B89, 213-218 (1994).
110. C. G. Ryan and D. N. Jamieson, *Nucl. Instr. Methods* B77, 203-214 (1993).
111. C. A. Heinrich and C. G. Ryan, Mineral paragenesis and regional zonation of granite-related Sn-As-Cu-Pb-Zn deposits, a chemical model for the Mole Granite district (Australia) based on PIXE fluid inclusion analyses, In: Water-Rock Interaction, Kharaka & Maest, Eds., *Balkema*, Rotterdam, pp. 1583-1587, (1992).
112. C. G. Ryan, C. A. Heinrich, T. P. Mernagh, *Nucl. Instr. Methods* B77, 463-471 (1993).
113. J. B. Lowenstern, G. A. Mahood, M. L. Rivers, S. R. Sutton, *Science* 252, 1405-1408 (1991).
114. D. D. Hickmott and W. S. Baldrige, *Econ. Geol.*, 90, 246-254 (1995).
115. J. R. Chen, H. Kneis, B. Martin, R. Nobile, K. Traxel, E. C. T. Chao, J. A. Minkin, *Nucl. Instr. Methods* 181, 151-157 (1981).
116. M. Vajic, M. Jaksic, S. Fazinic, V. Valkovic, G. W. Grime, F. Watt, *Nucl. Instr. Methods* B49, 336-339 (1990).
117. J. R. Chen, N. Martyrs, E. C. T. Chao, J. A. Minkin, C. L. Thompson, A. L. Hanson, H. W. Kraner, K. W. Jones, B. M. Gordon, R. E. Mills, *Nucl. Instr. Methods* B231, 241-245 (1984).
118. R. N. White, J. V. Smith, D. A. Spears, M. L. Rivers, S. R. Sutton, *Fuel* 68, 1480-1485 (1989).
119. A. Kolker and C.-L. Chou, *J. Geol.* 102, 111-116 (1994).
120. S. Bajt and K. Traxel, *Nucl. Instr. Methods* B54, 317-324 (1991).
121. K.-U. Braun-Dullaeus and K. Traxel, *Planet. Space Sci.*, 43, 429-434 (1995).
122. D. Hickmott and F. S. Spear, *Journ. of Petrol.*, 33, 965-1005 (1992).
123. W. J. Teesdale and J. L. Campbell, *Nucl. Instr. Methods* B77, 405-409 (1993).
124. R. Protz, W. J. Teesdale, J. A. Maxwell, J. L. Campbell, C. Duke, *Nucl. Instr. Methods*, B77, 509-516 (1993).
125. W. Woelfli, H. A. Polach, H. H. Anderson, H. H., Proc. Third Int. Conf. on Accelerator Mass Spectrometry, Zuerich, Switzerland *Nucl. Instr. Methods Phys. Res.* B5, 91-448 (1984).
126. H. E. Gove, A. E. Litherland, D. Elmore, Proc. Fourth Int. Conf. on Accelerator Mass Spectrometry, Niagara on the Lake, Ontario, Canada (1987), *Nucl. Instr. Methods* B29, 1-455, (1987).
127. F. You and G. M. Raisbeck, Proc. Fifth Int. Conf. on Accelerator Mass Spectrometry, Paris, France (1990), *Nucl. Instr. Methods Phys. Res.* B52, 211-630, (1990).
128. L. K. Fifield, D. Fink, S. H. Sie, C. Tuniz, Proc. Sixth Int. Conf. on Accelerator Mass Spectrometry, Canberra-Sydney, Australia (1993), *Nucl. Instr. Methods Phys. Res.* B92, 1-524, (1993).
129. K. H. Purser, *Nucl. Instr. Methods Phys. Res.* B92, 201-206, (1994).
130. C. Tuniz, D. Fink, M. A. C. Hotchkis, G. E. Jacobsen, E. M. Lawson, A. M. Smith, J. R. Bird, J. W. Boldeman, *Nucl. Instr. Methods Phys. Res.* B92, 22-26, (1994).
131. G. M. Raisbeck, F. You, M. Fruneau and J. M. Loiseaux, *Science* 202, 215-217, (1978).
132. G. M. Raisbeck and F. You, *J. Phys.* 40, 241-244 (1979).
133. Mao-Bai Chen, De-Ming Li, Sen-Liu Xu, Guo-Sheng Chen, Li-Gong Shen, Ying-Ji Zhang, Xiang-Shun Lu, Wei-Yu Zhang, Yue-Xiang Zhang and Zong-Kun Zhong, *Nucl. Instr. Methods Phys. Res.* B92, 213, (1994).
134. F. D. McDaniel, J. M. Anthony, S. N. Renfrow, D. Kim, S. A. Datar and S. Matteson, *Nucl. Instr. Methods Phys. Res.* B99 537-540, (1995).
135. J. C. Rucklidge, G. C. Wilson and L. R. Kilius, *Nucl. Instr. Methods Phys. Res.* B52, 507, (1990).
136. U. Fehn, G. R. Holdren, D. Elmore, T. Brunelle, R. Teng and P. W. Kubik, *Geophys. Res. Lett.* 13, 137, (1986).
137. M. H. Studier, C. Postmus, J. Mech, R. R. Walters and E. N. Sloth, *J. Inorg. Nucl. Chem.* 24, 755, (1962).
138. J. Rucklidge, L. Kilius and R. Fuge, *Nucl. Instr. Methods Phys. Res.*, B92, 417-420, (1994).
139. L. R. Kilius, A. E. Litherland, J. C. Rucklidge and N. Baba, *Appl. Radiat. Isot.* 43, 27, (1992).
140. G. M. Milton, H. R. Andrews, S. E. Causey, L. A. Chant, R. J. Cornett, W. G. Davies, B. F. Greiner, V. T. Koslowsky, Y. Imahori, S. J. Kramer, J. W. McKay and J. C. D. Milton, *Nucl. Instr. Methods Phys. Res.* B92, 376-379, (1994).
141. S. H. Sie and G. F. Suter, *Nucl. Instr. Methods Phys. Res.*, 221-226 (1994).
142. X. L. Zhao, M. J. Nadeau, L. R. Kilius, A. E. Litherland *Nucl. Instr. Methods Phys. Res.* B92, 249, (1994).
143. K. H. Purser, L. R. Kilius, A. E. Litherland and X. Zao, *Nucl. Instr. and Meth., Phys. Res.* B113, 445 (1996).
144. A. M. Smith, D. Fink, M. A. C. Hotchkis, G. E. Jacobsen, E. M. Lawson, C. Tuniz, E. Sacchi, D. Louvat, G. M. Zuppi and R. Bonetti, *Nucl. Instr. and Meth., Phys. Res.* A382, 309 (1996).